New Calibration Sources for Very Long Baseline Interferometry at 1.6 GHz

Author:
Mekuanint Kifle Hailemariam

Supervisor:
Dr. Michael Bietenholz
Dr. Aletha de Witt
Prof. Roy Booth

A thesis submitted in partial fulfilment of the requirements for the degree of Master of Science in Physics

in the

Faculty of Natural & Agricultural Sciences
University of Pretoria
Pretoria

July 2016

Declaration of Authorship

I, Mekuanint Kifle Hailemariam, declare that the thesis, which I hereby submit for the degree of Master of Science in Physics, at the University of Pretoria, is my own work and has not previously been submitted by me for a degree at this or any other tertiary institution.

SIGNATURE: .....
DATE: .....

UNIVERSITY OF PRETORIA

Abstract

Department of Physics
Faculty of Natural & Agricultural Sciences
University of Pretoria
Pretoria

Master of Science in Physics

New Calibration Sources for Very Long Baseline Interferometry at 1.6 GHz

by Mekuanint Kifle Hailemariam

I present new 1.6 GHz VLBI observations of sample of 43 radio sources in the Southern celestial Hemisphere. My goals were firstly to establish the suitability of the 43 sources as calibrators for 1.6 GHz VLBI observations, and secondly to determine, based on some selected sources from the sample, how the properties of the sources seen at 8.4 GHz are related to those seen at 1.6 GHz. I used seven telescopes; ASKAP, ATCA, Ceduna, Hobart, Mopra and Parkes from Australia, and HartRAO from South Africa.

By evaluating the sources' radial extents, flux density of the central components of the sources and their brightness, I classified the sources into very good, good, intermediate and bad calibrators. Among the 43 sources, I found that 38 sources fell into the good or very good calibrator classes. Among 35 of our sources, which are known to be good calibrators at 8.4 GHz, I found that 32 sources fell into the good or very good calibrator classes. Of the basis of my sample therefore, I can say that 91 percent of the good calibrators at 8.4 GHz are also safe to use at 1.6 GHz.

Acknowledgements

First and foremost I would like to express my sincere gratitude to Dr. Michael Bietenholz for his unlimited support on my research. I appreciate his patience, motivation, enthusiasm, immence knowledge and his ideal way of supervision. No words to thank him.

I wish to express my sincere thanks to Dr. Aletha de Witt, for her kind and continuous support and for providing me with all the necessary facilities and an excellent working environment for doing my research at HartRAO. I would like to express my deepest gratitude to Prof. Roy Booth, for his support and facilitate my studies at university of Pretoria.

I would like to thank Prof. Chris Theron and Ms. Elfrieda Meyburgh for their kind cooperation at the department of physics and made my way smooth.

I take this opportunity to express gratitude to Glenda Coetzer, Joseph Chefu, Gaaratwe Dibetle and all of HartRAO members for their contribution to made my stay at HartRAO very interesting and enjoyable.

I would also like to thank my friends Sayan Basu, Arvind Ramessur and Denise Dale for their direct and/or indirect help on my research work and out side my research.

This research was supported by the National Space Science Programme (NASSP) and Hartebeesthoek Radio Astronomy Observatory (HartRAO). The financial assistance of National Research Foundation (NRF) towards this research is hereby acknowledged.

Finally thanks goes to my parents for the unceasing encouragement, support and attention, and special thank to my sister Kelebet Kifle for her support and encouragement during my study.

Contents

List of Figures

List of Tables

This thesis is dedicated to the memory of my aunt
Merkeb Hailemariam

Chapter 1

Introduction

Relatively few Very Long Baseline Interferometry (VLBI) calibrator sources are known in the Southern Hemisphere especially in the 1.4 GHz band (L-band; 1-2 GHz). This is mainly due to the smaller number of observing facilities in the south than in the north. There are different surveys undergoing to increase the number of calibrator sources in the Southern Hemisphere but most of the surveys are focused on observations at frequencies higher than 2 GHz for example 8.4 GHz (X-band) and 2.3 GHz (S-band) (e.g. Petrov et al. 2011; Hungwe et al. 2011), and there are virtually no VLBI calibrator observations at frequencies <2 GHz. The small number of known calibrator sources and antennas in the southern hemisphere makes VLBI observation more difficult.

Most VLBI observations, which enable us to study astronomical sources with milliarcsecond and sub-milliarcsecond resolution, rely on observations of calibrator sources. We use the calibrator sources to determine any gain and/or phase change as the emitted signals from radio sources travel through the atmosphere and antenna system. Once the gains are determined they will be used to make corrections on the observed data of our target source (the source we are interested to study).

Almost all calibrator sources used for VLBI are extra-galactic radio sources, thought to be due to the accretion of material onto supermassive black holes in distant galaxies. As matter accretes onto the black hole, highly energetic particles are ejected due to the magnetic field of the black hole which in turn produces relativistic jets which can be observed at radio frequencies. The size of these relativistic jets of good calibrator sources are small in the sense that they are unresolved with the longest baseline we have and appear point like.

New VLBI-capable telescopes are coming to the south, in particular operating at <2 GHz. ASKAP (<2 GHz only) and MeerKAT (< 2 GHz and higher frequencies), which

are pathfinders for the Square Kilometer Array (SKA). The SKA is currently being built by Australia and South Africa respectively. MeerKAT will be the most sensitive centimeter wavelength instrument in the Southern Hemisphere. Further information, including the description of the specific science programs for MeerKAT and ASKAP is found in Booth et al. (2009) and Johnston et al. (2008) respectively. The SKA in turn will be the world's largest and most sensitive radio telescope when it is completed.

Despite the increasing number of antennas in the Southern Hemisphere and the future plans to study different astrophysical phenomenon at lower frequencies, the number of calibrator sources for 1.4 GHz band observations are very few. The high demand for calibrator sources especially in the future is the major motivation to look for calibrator sources in the 1.4 GHz band.

This thesis involves reducing and analyzing of VLBI observations of 43 sources in the Southern Hemisphere at 1.6 GHz. Some of the sources were already observed at 8.4 GHz and found to be good calibrators at this observing frequency. The goals of the work described in this thesis are firstly to establish the suitability of the 43 sources as calibrators in the 1.4 GHz band, and secondly to determine, based on some selected sources from the sample, how the properties of the sources at one frequency are related to the properties at another. Finally, it would increase the number of known calibrator sources in the 1.4 GHz band in the Southern Hemisphere. We will also determine how safe it is to use sources which are good calibrator sources at higher frequencies, as calibrator sources at lower frequencies. This kind of study of calibrator sources at a different frequency also contributes to the understanding of source morphology over a wider range of frequencies.

The thesis chapters are organized as follows: the next chapter provides an overview of the basics of radio interferometry. Chapter three discusses the need for and techniques of calibration, and have a discussion on calibrator sources and previous results. Chapter four explains the different steps in the data reduction process. In chapter five I present my results, and I give a summary and conclusion of my work in chapter 6.

Chapter 2

Basics of Radio Interferometry

Radio telescopes are used to study astronomical objects by collecting the radio waves emitted by these sources. These telescopes are designed in different sizes and shapes. A key feature of a telescope is its angular resolution. This is a telescope's ability to distinguish between sources lying close together on the sky and is given by

$$\theta = 1.22\frac{\lambda}{D} \tag{2.1}$$

where θ is the angular resolution in radian, λ is the wavelength and D is the diameter of the telescope. Both λ and D are expressed in the same units.

Early discoveries in radio astronomy were made with single telescopes with resolutions of a degree or so but there are many celestial radio sources with smaller angular size. Radio astronomers use interferometry, which uses two or more antennas separated by some distance, to observe these small angular size sources. The resolution of radio interferometry depends on the wave length of observation and the maximum baseline in the interferometer, and is given by

$$\theta = 1.22\frac{\lambda}{B} \tag{2.2}$$

where B is the maximum baseline length. For example, the observations we describe later, which are at a frequency of 1.6 GHz and therefore a wavelength of 18.75 cm, have a maximum baseline of 55 Megawavelength, and a full width at half maximum (FWHM) resolution of 4.6 milliarcsecond.

2.1 How interferometry works

If we consider two antennas (antenna A and B, as illustrated in Figure 2) observing the same source, which is point like and in the far field (i.e the incident wave front can be considered to be a plane) of the interferometer, then the signal from the source will arrive first at antenna B and then at antenna A. The extra distance, x, that the signal travels to arrive at antenna A, is called the geometric delay. One of the most important parameters which can be derived from interferometric observations is the geometric delay τ_g. If we ignore the atmospheric and other delays and assume a narrow bandpass, allowing only signal components very close to the observing frequency, then the geometric delay is given by

$$\tau_g = \frac{x}{c} = \frac{d\cos\theta}{c}, \tag{2.3}$$

where c is the speed of light. As the telescopes track the source, the delay is constantly changing, because the projected baseline vector (b=dsin θ) or θ is changing. The geometric delay for the longest baseline in our observation (ATCA and HartRAO) could vary between 0 and $\sim$ 33 milliseconds depending on where our source is located relative to the two telescopes.

The phase difference Φ between the signals received at telescope A and B is dependent on the geometrical delay and the observing wavelength and is given by

$$\Phi = 2\pi\nu\tau_g = \frac{2\pi\nu}{c} d\cos\theta = \frac{2\pi d}{\lambda}\cos\theta \tag{2.4}$$

The output voltages as a function of time t from the two antennas are

$$V(t)_A = V_A\cos(2\pi\nu(t-\tau_g)) \tag{2.5}$$

and

$$V(t)_B = V_B\cos(2\pi\nu t) \tag{2.6}$$

The voltage from the two antennas are multiplied and then time averaged by the correlator. If we introduce the instrumental delay τ_i and assuming identical antennas ($V_A = V_B$=V), the output of the correlator can be written in terms of τ =τ_g - τ_i as:

$$r(\tau) = \frac{V^2}{2}\cos(2\pi\nu\tau) \tag{2.7}$$

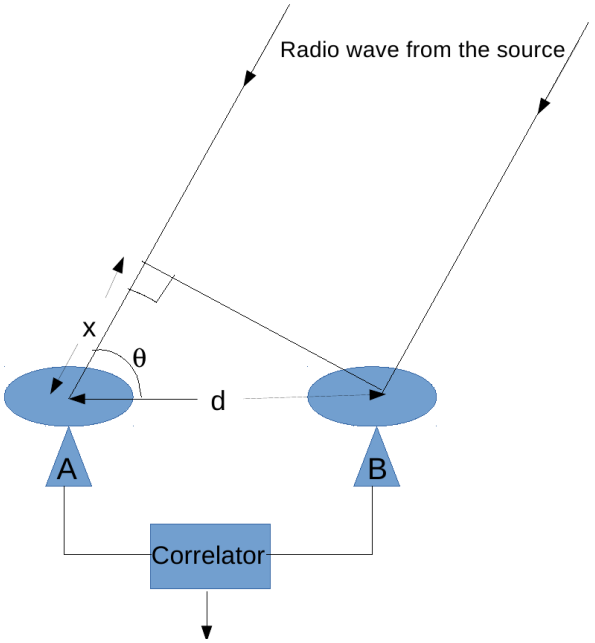

FIGURE 2.1: Two antennas observing the same source at a very far distance. d is the baseline length, x is the extra distance the wave travels to arrive antenna A compared to antenna B and θ is the angle between the incoming radio wave and the baseline.

For a point source at a position $\theta_s = \theta_0 + \theta'$, where θ_0 is the pointing center (i.e. pointing direction of the antenna), the geometric delay will be

$$\tau_g = \frac{d\cos(\theta_0 + \theta^{'})}{c} \tag{2.8}$$

Then the output of the correlator for small $\theta^{'}$ will be

$$\begin{aligned} r(\tau) &= \frac{V^2}{2}\cos\{2\pi\nu[\frac{d}{c}\cos(\theta_0 + \theta^{'}) - \tau_i]\} \\ &\approx \frac{V^2}{2}\cos\{2\pi\nu[\frac{d}{c}(\cos\theta_0 - \sin\theta_0\sin\theta^{'}) - \tau_i]\} \end{aligned} \tag{2.9}$$

When the signals are added, they interfere with each other either constructively to produce a strong signal or destructively to produce a weaker signal. The information about the intensity and the structure of the radio sources will be determined based on this constructive and destructive interference of the radiation.

For two identical, fixed and isotropically receiving antennas the power received is given by (Wohlleben et al., 1991)

$$P_r(\theta) = \frac{\vec{E}\vec{h}^2(\theta)}{8R_r}(1 + cos\Phi) \tag{2.10}$$

where $\vec{E}$ is the electric field of the source at the antenna element, $\vec{h}$ is the effective vectorial complex height of the appropriate element and R_r is the radiation resistance of one antenna.

2.1.1 Autocorrelation and cross-correlation

The output of a correlator could be autocorrelated or cross-correlated. The auto-correlation is correlation (i.e. multiplied and time averaged) of a signal with itself at different points in time. The output of autocorrelated signal with input voltage V(t) is given by

$$r_{auto} = \langle V(t)V(t-\tau)\rangle \tag{2.11}$$

The Fourier transform of the autocorrelation function is called the power spectrum of the signal input to the correlator and is given by

$$S_{VV}(\nu) = \int_{-\infty}^{\infty} r_{auto}(\tau)e^{-i2\pi\tau\nu}d\tau \tag{2.12}$$

Cross-correlation is correlation of two different signals as function of time lag applied to one of them. The correlator output for two input voltages $V_1(t)$ and $V_2(t)$ is

$$r_{cross} = \langle V_1(t)V_2(t-\tau)\rangle \tag{2.13}$$

and the cross power spectrum is given by

$$S_{V_1V_2}(\nu) = \int_{-\infty}^{\infty} r_{cross}(\tau)e^{-i2\pi\tau\nu}d\tau \tag{2.14}$$

2.2 Relation between visibility and intensity

For a very distant celestial radio source located at a position $\mathbf{R}$, producing a time variable electric field $\mathbf{E}(\mathbf{R},t)$, the general form of the electric field at frequency ν is given by

$$\mathbf{E}_\nu(\mathbf{r}) = \int \frac{\mathbf{E}(\mathbf{R})\mathbf{e}^{\mathbf{2\pi i\nu}\frac{|\mathbf{R}-\mathbf{r}|}{\mathbf{c}}}}{|\mathbf{R}-\mathbf{r}|}\mathbf{dS}. \tag{2.15}$$

The correlation of the field at two points $\mathbf{r_1}$ and $\mathbf{r_2}$ is defined as

$$\mathbf{V}_\nu(\mathbf{r_1},\mathbf{r_2}) = \langle \mathbf{E}_\nu(\mathbf{r_1})\mathbf{E}^*_\nu(\mathbf{r_2})\rangle. \tag{2.16}$$

Under the assumption that the radiation from the astronomical object is not spatially

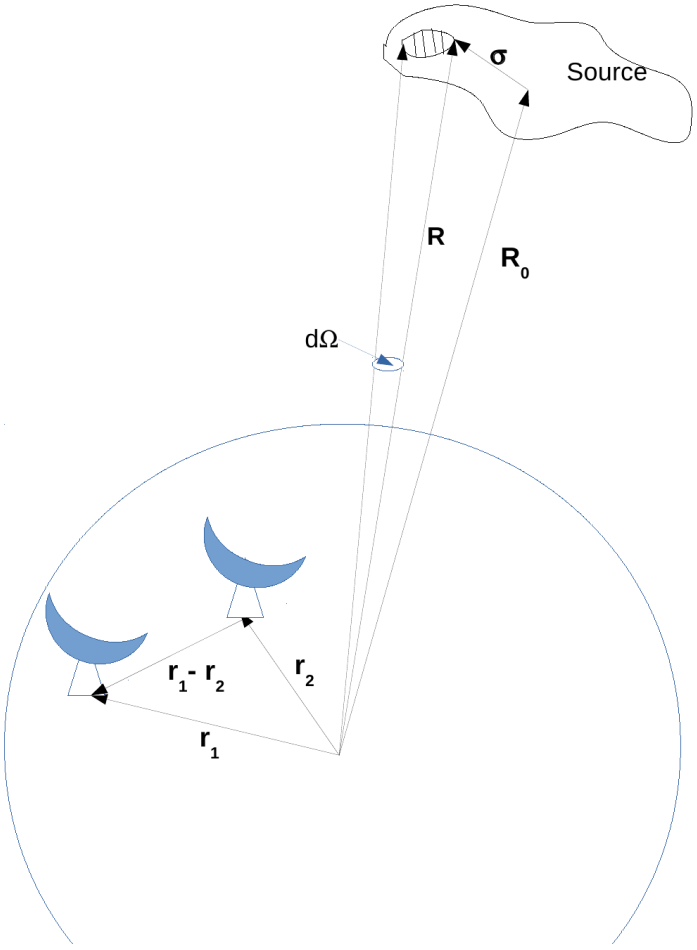

FIGURE 2.2: A simple interferometer and radio source. $\mathbf{r_1}$ and $\mathbf{r_2}$ are distances from the center (we measure the coordinates) to the two telescopes, $\mathbf{R_0}$ is a distance from the center to the phase center of the source, $\mathbf{d\Omega}$ is the solid angle of small element on the source and σ is a distance from the phase center to the small element on the source

.

coherent (i.e $\langle \mathbf{E}_\nu(\mathbf{r_1})\mathbf{E}^*_\nu(\mathbf{r_2})\rangle = \mathbf{0}$, for $\mathbf{R_1} \neq \mathbf{R_2}$) and $\mathbf{r} \ll |\mathbf{R}|$, the coherence function $\mathrm{V}_\nu(\mathbf{r_1}, \mathbf{r_2})$ of the field can be written as (Clark, 1999)

$$V_\nu(\mathbf{r_1}, \mathbf{r_2}) = \int \mathbf{I}_\nu(\mathbf{s}) \mathbf{e}^{-\mathbf{2\pi i \nu s.(r_1 - r_2)/c}} \mathbf{d\Omega} \tag{2.17}$$

Where $\mathbf{s}$ is a unit vector in the direction of $\mathbf{R}$ (i.e. $\mathbf{s} = \frac{\mathbf{R}}{|\mathbf{R}|}$) and I_ν is the observed intensity of the radiation field given by

$$I_\nu = \frac{\mathbf{R^2}}{\langle |\mathbf{E}_\nu| \rangle^{\mathbf{2}}} \tag{2.18}$$

In a more convenient way we can write the spatial coherence function as function of the spatial frequencies u and v. These are the coordinates that represent the spacing of

the antennas with respect to the phase tracking center $\mathbf{s_0} = \frac{\mathbf{R_0}}{|\mathbf{R_0}|}$ as (Thompson, 1999; Thompson et al., 2007).

$$V_\nu(u,\upsilon) = \int\int I_\nu(l,m)e^{-2\pi i(ul+\upsilon m)}dldm \tag{2.19}$$

The spatial frequencies of visibilities u and υ are the length of the baseline divided with the observed wavelength, so they are non-dimensional values. The l and m are projections of a unit vector in the direction of $\mathbf{s}$ on (u,υ) axes. Since the above equation is a Fourier transform, we can invert it to get the intensity distribution of the radiation as

$$I_\nu(l,m) = \int\int V_\nu(u,\upsilon)e^{2\pi i(ux+\upsilon y)}dud\upsilon \tag{2.20}$$

In practice we can't measure the spatial coherence function everywhere, instead we take samples at particular places on the u-υ plane. Therefore, the intensity distribution will be

$$I_\nu^D(l,m) = \int\int V_\nu(u,\upsilon)S_\nu(u,\upsilon)e^{2\pi i(ux+\upsilon y)}dud\upsilon \tag{2.21}$$

Where $S_\nu(u,\upsilon)$ is a sampling function, which is zero where no data have been taken. $\mathrm{I}_\nu^D(x,y)$ is called the dirty image, which is the convolution of I_ν(l,m) with the synthesized beam B(l,m), where B(l,m) is given by

$$B(l,m) = \int\int S_\nu(u,\upsilon)e^{2\pi i(ux+\upsilon y)}dud\upsilon \tag{2.22}$$

The term $\mathrm{V}_\nu(u,\upsilon)$ is normally termed as the complex visibility relative to the phase tracking center, which is the property of the radiation field that we want to measure using our interferometer.

In interferometric observations we measure visibilities of various spatial frequencies and make an image of them. Wider range of the spatial frequencies or the uv coverage provides us better spacial resolutions and vice versa.

Chapter 3

Calibration and Calibrator Sources

3.1 Why we need calibration

Things such as geometrical errors or atmospheric propagation delay will cause the measured visibility to differ from the true one, which is the one that would be observed by a perfect interferometer above the atmosphere. Through calibration we try to recover the true visibilities from the measured ones. Both the phase and the amplitude of the visibilities are generally affected. The visibility phase is mainly affected by geometrical and instrumental errors and atmospheric and ionospheric effects. In this section I give an overview of the factors that affect the visibility and what we need to consider during calibration.

From now on I will represent the true visibility from two antennas i and j by $\mathrm{V}_{i,j}^{T}$(u,v) and the observed visibility by V_{ij}^{M}(u,v). A well designed array satisfies a linear relationship between the measured and the true visibility and we can write the basic calibration formula as

$$V_{ij}^{M} = G_{ij}V_{ij}^{T} + \epsilon_{ij}(t) + \eta_{ij}(t) \tag{3.1}$$

where G_{ij} is the complex gain for the i-jth baseline, ϵ_{ij}(t) is the baseline based complex offset, η_{ij} is a stochastic complex noise and t is the time of observation. Further explanation on this can be obtained from Fomalont & Perley (1999); Moran & Dhawan (1995)

The basic calibration process involves delay (phase) calibration and amplitude calibration. The origin of delay errors are due to geometric errors related to errors in the terrestrial coordinates of the antennas and/or celestial coordinates of the source, and

instrumental errors due to electronics at each antenna. Errors in the antenna coordinates can arise from inaccurate antenna positions, movement of antennas due to tectonic plate motion, irregular and periodic shifts of the earth's rotation axis. Errors in celestial coordinates arise from inaccurate source position and an inadequate model of precession and nutation of Earth's rotation axis.

Instrumental delay errors are introduced at the antenna when the frequency standards that control the station clock are not exactly set to the desired frequency. Any differences between clocks in a baseline will introduce a change in the delay error with time, which will result in the phase also changing with time. Instrumental delay errors can also be caused by offsets between the rotation axes of antennas and due to structural changes in the relative separation of dish components due to changing gravitational stresses as the antenna tracks the source.

Modern arrays operate over a large bandwidths to get a better signal-to-noise ratio for weaker sources. Large bandwidth causes a phase difference between the ends of the band since the period is different at different frequencies. The phase shift or phase difference ($\Delta\phi$) across a band width of $\Delta\nu$ as a result of the net residual delay $\Delta\tau$ is given by

$$\Delta\phi = 2\pi\Delta\nu\Delta\tau \tag{3.2}$$

To minimize the effect due to delay between signals, the delay must be small so as to keep the phase shift across the band width smaller than one radian. In addition to the phase shift across the band, the delay rate (the change in delay with time) causes a phase shift over a scan or observing time. Delay calibration normally refers to the estimation of these small residual delays and the solution is then applied to the target source/s to remove the effect.

In addition to delays and rates, large phase errors occur due to atmospheric and ionospheric effects. When radio signals propagate through the Earth's atmosphere, the signal will be affected in different ways. Due to the refractive index of the atmosphere the radio wave path length will increase and will modify the phase. Atmospheric refractivity is dependent on the physical parameters of air such as pressure, temperature and water content. It varies in space and time as well, due the physical processes in the atmosphere. The estimation of the excess path length is given by Fomalont & Perley (1999)

$$L = 0.228P_{tot} + 6.3\omega \tag{3.3}$$

where P_{tot} is the total ground level pressure in millibars, ω is the vertical column water vapor content above the antenna in cm, and L is the total zenith excess path in centimeter. Along any particular line of sight, the additional path length differs for

different azimuth angle and altitude. It becomes larger for low elevations and altitude. In addition to the atmosphere, the ionosphere affects the path length and distorts the phase of the radio wave passing through it.

I have discussed the different mechanisms affecting the visibility delay (phase): geometric errors related to the terrestrial coordinates of the antennas and/or celestial coordinates of the sources, instrumental errors due to electronics at each antenna, atmospheric and ionospheric effects when the wave passes through the atmosphere. All these contributes to the phase delay known as the total delay.

The correlator tries to remove these delays using a delay model, but, since the model only includes a seasonal average model of the atmosphere, and can therefore not account for local or day to day changes, the visibilities generated by the correlator contain residual phase errors which can be expressed as

$$\phi_{corr} = \phi_{\nu}(t,\nu) + \phi_{inst}(t,\nu) + \phi_{geom}(t,\nu) + \phi_{atm}(t,\nu) + \phi_{ion}(t,\nu) \tag{3.4}$$

where ϕ_{ν} is true visibility phase, ϕ_{inst} is the sum of any residual instrumental phase errors, ϕ_{geom} is the residual phase error due to geometric errors, ϕ_{atm} and ϕ_{ion} are the neutral atmospheric and ionospheric delays above each antenna respectively. The dominant error source in radio interferometry is tropospheric delay error for observing frequencies $\geq$ 10 GHz, and ionospheric delay for lower frequencies. The ionospheric dispersive delay is very important especially at low frequency observations below 2 GHz (NRAO, 2014).

The observed visibility amplitude is affected primarily by aperture efficiency, atmospheric absorption and pointing errors. When the atmosphere absorbs radio waves it decreases the signal strength of the source, while atmospheric emission contributes to the noise temperature of the system. The antenna pointing error is the difference between the actual pointing position (i.e. the location of the center of the primary beam) and the desired position, and this can cause reduced sensitivity.

Once we know what affects our visibility the next step is to remove all the effects using different software packages designed for the data reduction and calibration. The well known software packages to calibrate interferometric data are AIPS, MIRIAD, CASA and GIPSY.

3.1.1 What type of sources are used as calibrators

An ideal calibrator would look the same on all observing baselines, which means that it has to be unresolved on all baselines. A good calibrator source should be strong

enough to be detectable on all baselines with sufficient signal-to-noise ratio to derive an unambiguous solution. Along with brightness and compactness measurements, position measurements of sources are important to use them as calibrators. Precise measurement of the position and movement of of stars and other celestial bodies is called astrometry, and VLBI astrometry allows us to determine source position with sub-milliarcsecond accuracy. Delay errors we discussed in the previous section would affect accurate position measurements.

Most VLBI calibrator sources are not completely unresolved or point-like, but are dominated by a point like component (or core dominated). Astronomers use these core dominated sources as calibrators because most of the flux is concentrated in the central component. Compactness measures how much of the flux is concentrated at the central component. When we speak about the compactness of a source it is always relative to the resolution of our interferometer. The same source could be compact for lower angular resolution observations and could look extended for higher angular resolution observations. Good calibrator sources should be unresolved with our longest baseline.

The structure of a source can vary significantly with frequency, therefore, a source might be dominated by a compact core when observed at high frequencies and may show extended jet features when observed at low frequencies. This is one of the concerns of my thesis. The effect of source structure on the band width could be studied to determine the compactness of the source. This is done by calculating the structural index, which defines the astrometric quality of a radio source according to the median structure delay corrections (Fey & Charlot, 2000, 1997). We must choose calibrator sources appropriate for our observing frequency.

Different calibrators are chosen depending on the type of calibration. Preferably point like sources near the target source are used for gain and phase calibration, where as bandpass calibration can be done using a strong sources which is not necessarily point like or near the target source.

In some cases we can use our target sources as its own calibrator and do self-calibration. Self calibration is a powerful technique to calibrate our data if our sources are observed with a high signal-to-noise ratio and sufficient number of antennas. The problem with self-calibration is that information about the absolute position and the absolute flux density of the source will be lost.

Almost all calibrator sources used for VLBI are extra-galactic radio sources. They are very distant objects and therefore, generally, have no discernible proper motions on the sky.

3.1.2 Why we need calibrator sources

When self-calibration is not possible, we need to use calibrator sources, which are known to be compact and have an accurate known position. Calibrators are also important in many other applications like differential astrometry, space geodesy and space navigation.

Calibrator sources are sources that have known properties and we therefore know how they should behave during an observation. Any deviation of the observed visibility from the true one could be because of the different gains and delays during an observation. The gains and delays should be calculated in the calibration process and then applied to our target sources.

A calibrator source should be separated from the target source by as small an angle as possible in order to look along the same line-of-sight through the atmosphere, and therefore many calibrators are required. Especially, the VLBI observing capabilities in the Southern Hemisphere need a large number of calibrator sources at different frequencies as the number of known calibrator sources in the Southern Hemisphere is small compared to the number of known calibrator sources in the Northern Hemisphere.

3.1.2.1 Extra-galactic radio sources

The extra-galactic radio sources ranges from normal galaxies like our own Galaxy, the Milky Way, in which the radiative power output is roughly equal to the combination of the radiation from the stars in the galaxy, to galaxies which have much greater luminosities than normal galaxies of comparable size. This high luminosity is due to the emission that originates from a very small central region of an active galaxy called the active galactic nucleus (AGN). The radiative power from their nuclei can outshine the stellar population by up to a thousand times (Schneider, 2006). Intermediate in luminosity are the less powerful FR-I[1] radio galaxies, the radio quiet quasars, and galaxies with active star formation.

AGNs are classified in to different groups depending on their spectral properties, luminosity and their ratio of the nuclear luminosity to that of the the luminosity from the stars in the galaxy. Quasars are the most luminous AGNs, and are observed out to the highest measured red shift.

[1]The Fanaroff-Riley classification is a scheme created by B.L. Fanaroff and J.M. Riley in 1974, which is used to distinguish radio galaxies with active nuclei based on their radio luminosity or brightness of their radio emissions in relation to their hosting environment. Class I (abbreviated FR-I) are sources whose luminosity decreases as the distance from the central galaxy or quasar host increases, while Class II (FR-II) sources exhibit increasing luminosity in the lobes (Fanaroff & Riley, 1974).

The energy source of an AGN is the accretion of matter onto a super massive black hole. The highly energetic particles from AGNs produce non-thermal radiation, which is produced as a result of acceleration of energetic particles due to the magnetic field.

The morphology of extra galactic radio sources is often described in terms of two components called the extended (i.e spatially resolved) and compact components (i.e. spatially unresolved). These compact components are characterized by small angular sizes ($\ll$ 1 arcsecond), high surface brightness with peak brightness temperature $\sim 10^{12}$ K, variability on characteristic scales of months to years and flat (i.e the flux density is independent of frequency) or inverted spectra (i.e the flux density increases towards shorter wavelengths, Kellermann & Pauliny-Toth (1981)). Most of the time compact sources show self absorption whereas the extended components are optically thin to its own radio synchrotron emission.

Depending on the percentage of the flux density in the compact component, radio sources are classified into compact or extended. Core dominated sources, which are good candidates for calibrator sources, have most of their flux density in the compact component of the source. The radio emission from Radio galaxies is primarily from extended lobes or jets with inverted power law spectra, whereas AGNs have flat or inverted radio spectra characteristic of an opaque synchrotron source.

3.1.3 Calibrator surveys

Most of the calibrator sources identified in the Southern Hemisphere were observed during geodetic experiments. The campaigns of Fey et al. (2004) and Fey et al. (2006) provided milliarcsecond accurate positions of 56 Southern Hemisphere radio sources to increase the sky density of Southern Hemisphere sources in the International Celestial Reference Frame (ICRF)[2] and to provide additional phase-reference sources with accurate positions for use in astrophysical observations. These campaigns were the largest in providing new milliarcsecond accurate astrometric positions for ICRF sources at declination south of -30^0.

At this time there are different observing programs underway, which focus on searching for calibrator sources in the southern sky. The LBA calibrator survey (LCS) is a big campaign to observe a list of candidate flat spectrum radio sources with declinations south of -30^0 at 8.4 GHz using the Australian Long Baseline Array (LBA) instrument. The aim of the campaign is to determine the position of compact extra-galactic radio

[2]The International Celestial Reference Frame (ICRF) realizes a reference system, the International Celestial Reference System (ICRS), by precise equatorial coordinates of extra-galactic radio sources observed in Very Long Baseline Interferometry (VLBI) programs.

sources with milliarcsecond accuracy, their correlated flux density and their suitability as calibrators for phase referencing observations and as target for astrometry and geodesy observations.

The first LCS catalog (LCS1) by Petrov et al. (2011) contains accurate positions and correlated flux densities for 410 compact radio sources at 8.3 GHz. Petrov et al. (2011) also determined correlated flux densities for 111 calibrator sources in addition to the 410 target sources. The catalog spans declinations between -90^0 and -40^0 and has increased the number of compact radio sources in this declination range, with measured VLBI correlated flux densities and position known to milliarcsecond accuracy. In the LCS, positions of 1019 new objects have been determined from analysis of 16 VLBI experiments with the LBA so far. The latest update about LCS can be found on http://astrogeo.org/lcs/. Many other observations are carried out to increase the number of calibrator sources and most of them are at an observing frequency of 2.3 GHz, 8.4 GHz or higher.

Hungwe et al. (2011) presented a detailed multi-epoch analysis of 31 Southern Hemisphere radio sources with declinations between 0^0 and -60^0 at 2.3 GHz. They determined the compactness and variability of each source, and then classified all but three of the sources as very good calibrators.

Ojha et al. (2004) presented observations of 69 Southern Hemisphere extra-galactic sources in the International Celestial Reference Frame (ICRF) with the aim of evaluating the continued suitability of these sources for reference frame use based on their intrinsic source structure and structural variability. Even though more than half of the sources show extended structure in the form of multiple compact components they have most of their flux densities in the central component. The other sources exhibit compact structure, and they are well suited to use for a reference frame.

Chapter 4

Observations and Data Reduction

4.1 Observations

We selected our sample of 43 sources from the Radio Fundamental Catalog (RFC[1]) of compact radio sources (Beasley et al., 2002; Fomalont et al., 2003; Petrov et al., 2005, 2006; Kovalev et al., 2007; Petrov et al., 2008, 2011). In the catalog, we found 1131 sources with declination $< -30°$ and that had only been observed at 8.4 GHz. Of these, we found 77 sources with a flux density > 500 mJy that are listed as a suitable calibrator source. Among the 77 sources, we selected the 25 sources for which 8.4 GHz images are available and brightest 9 of the remainder. In order to cover all Right Ascensions for our 24-hour observations we also included 7 sources listed in the RFC as non-calibrator sources. We finally added two additional sources, one of which is listed as good calibrator in the catalog, to use as fringe finders.

We observed the sources at 1.6 GHz using the seven antennas listed in Table 4.1. We planned to observe using eight antennas including Tidbinbilla but this antenna failed to observe. The observations were carried out between 22 and 23 February 2015. We used 16 channels with each of width 0.5 MHz, 4 intermediate frequencies (IFs) and 4 correlations (RR, LL, RL and LR, where the R and L refers to right and left circular polarization). The scan length was 5 minutes and we obtained at least five scans per source.

Six of the seven antennas are located in Australia and one antenna is located at Hartebeesthoek Radio Astronomy Observatory (HartRAO), in South Africa. There is a large gap between the HartRAO and the antennas in Australia. This is clearly seen

[1]Available on the Web at http://astrogeo.org/rfc/. The source selection was made using the rfc_2013b version of the catalog

TABLE 4.1: Participating antennas

Antenna	Diameter	Frequency range
ASKAP (AK)	36 antennas (12m each)	0.7 - 1.8 GHz
ATCA (AT)	6 antennas (22m each)	1.1 - 110 GHz
Ceduna (CD)	30m	1.2 - 23 GHz
HartRAO (HH)	26m	1.66 - 23 GHz
Hobart (HO)	26m	1.2 - 23 GHz
Mopra (MP)	22m	0.3 - 100 GHz
Parkes (PA)	64m	0.7- 22 GHz

in uv plots of our visibilities, and Figure 4.1 shows the uv-coverage for 0454-810 as an example. Similar uv coverage was obtained for the other sources.

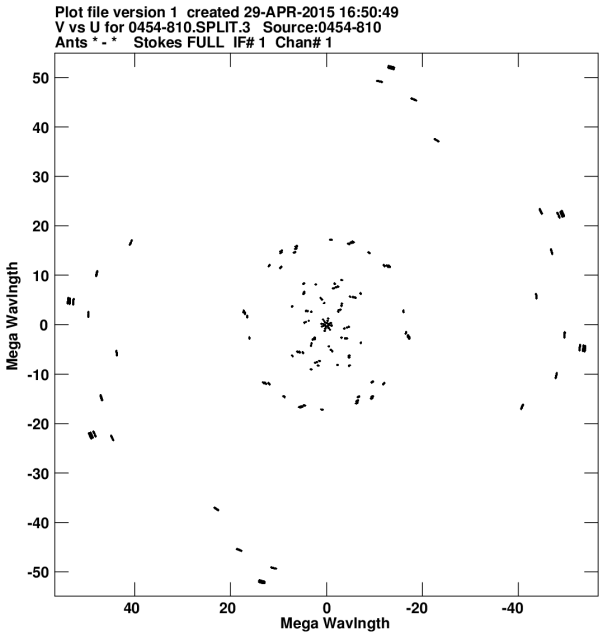

FIGURE 4.1: uv coverage for 0454-810. The uv-coverage around the center is for telescopes in Australia only, and the other after the gap is the uv-coverage of the HartRAO baselines

TABLE 4.2: Sources

ID	Sources (B1950 name)	Right Ascension[1] (J2000)	Declination[1] (J2000)	Type[2]	Redshift [2]
1	0056-572	00:58:46.5812	-56:59:11.470	Sy1	0.018
2	0252-549	02:53:29.1804	-54:41:51.436	Q	0.537
3	0312-770	03:11:55.2502	-76:51:50.848	Q	0.223
4	0334-546	03:35:53.9248	-54:30:25.115	Q	—
5	0454-810	04:50:05.4402	-81:01:02.231	Q	0.444
6	0530-727	05:29:30.0422	-72:45:28.507	PB	—
7	0743-673	07:43:31.6116	-67:26:25.546	Q	1.50998
8	0903-573	09:04:53.1794	-57:35:05.782	Sy1	0.695
9	1036-529	10:38:40.6569	-53:11:43.270	Q	—
10	1039-474	10:41:44.6498	-47:40:00.065	Q	2.558
11	1049-534	10:51:09.0999	-53:44:46.542	—	—
12	1059-631	11:01:54.3785	-63:25:22.595	Q	—
13	1105-680	11:07:12.6951	-68:20:50.727	Q	0.588
14	1109-567	11:12:07.2699	-57:03:39.745	—	—
15	1129-580	11:31:43.2880	-58:18:53.444	Q	—
16	1143-696	11:45:53.6241	-69:54:01.798	Sy1	0.243
17	1148-671	11:51:13.4265	-67:28:11.094	Q	—
18	1204-613	12:06:51.4961	-61:38:56.760	—	—
20	1249-673	12:52:43.2108	-67:37:38.745	Q	—
21	1251-713	12:54:59.9215	-71:38:18.437	Q	—
22	1312-533	13:15:04.1809	-53:34:35.889	—	—
23	1352-632	13:55:46.6120	-63:26:42.573	R	—
24	1420-679	14:24:55.5574	-68:07:58.095	Q	—
25	1424-418	14:27:56.2976	-42:06:19.438	Q	1.552
26	1509-564	15:12:55.8196	-56:40:30.642	—	—
27	1511-558	15:15:12.6731	-55:59:32.836	—	—
28	1619-680	16:24:18.4370	-68:09:12.497	Q	1.360
29	1624-617	16:28:54.6898	-61:52:36.398	AGN	2.578
30	1659-621	17:03:36.5412	-62:12:40.008	Q	1.747
31	1740-517	17:44:25.4503	-51:44:43.793	AGN	—
32	1758-651	18:03:23.4967	-65:07:36.761	G	1.991
33	1806-458	18:09:57.8717	-45:52:41.014	Q	0.06965
34	1831-711	18:37:28.7150	-71:08:43.555	Q	1.355998
35	1903-802	19:12:40.0192	-80:10:05.946	Q	0.500
36	1925-610	19:30:06.1601	-60:56:09.184	Q	3.254
37	1935-692	19:40:25.5282	-69:07:56.971	Q	3.152
38	2030-689	20:35:48.8765	-68:46:33.841	Q	1.084
39	2059-786	21:05:44.9614	-78:25:34.547	Q	—
40	2142-758	21:47:12.7306	-75:36:13.225	Q	1.139001
41	2146-783	21:52:03.1546	-78:07:06.639	Q	3.997
42	2300-683	23:03:43.5646	-68:07:37.443	Sy1	0.51581
43	2333-528	23:36:12.1446	-52:36:21.950	PB	—

[1] http://astrogeo.org/rfc/

[2] The SIMBAD astronomical database (Wenger et al., 2000). AGN (Active galaxy nucleus), BL (BL Lac-type object), G (Galaxy), PB (Possibly blazar), Q (Quasar), R (Radio source), Sy1 (Seyfert 1 galaxy), — (no information available).

4.2 Data reduction

I used the Astronomical Image Processing System (AIPS), version 31DEC13, software to reduce or calibrate the data. AIPS is a software package developed by the National Radio Astronomy Observatory (NRAO) for calibration, data analysis, imaging, plotting and performing a variety of ancillary tasks on astronomical data, primarily for radio astronomy.

The actual visibility values are baseline based, and each visibility always involves 2 antennas. The calibration process was antenna-based and it involves deriving the the complex antenna gains (i.e. at any given time there is one complex gain for each antenna).

During the calibration process, using AIPS, the raw data are never touched, all calibration information is stored in tables attached to the data file called extension files. These tables can be interpolated, extrapolated, merged, smoothed. A reference antenna is chosen, and the gain phases of the other antennas are all referred to that of the reference antenna, which is assumed to have gain phase of 0"

4.2.1 System temperature table preparation

I realized that there is no TY table which contains the measured system temperature (T_{sys}) of each antenna, and I had to prepare a T_{sys} table from the information available in the observing page http://www.atnf.csiro.au/vlbi/wiki/index.php?n=LBAFeb2014.V504A.

A T_{sys} table contains the antenna name, antenna gain, mounting description of the antenna and the degrees per flux unit (or Jy) (DPFU). Different stations write out system temperature differently, the units might not be the same for different stations. Sometimes the T_{sys} is given in degrees K, in which case we need the DPFU conversion factor, and sometimes the T_{sys} is given in Jy, in which case the DPFU conversion factor is just 1.0. The DPFU can be calculated using,

$$DPFU = \frac{T_{sys}}{SEFD} \tag{4.1}$$

Where SEFD is the system equivalent flux density (See table 4.3 for nominal SEFD values for each antenna). We want to get the right T_{sys} value assigned to every IF and polarization.

The measured values of the system temperature of each antenna can be found on the observing log of the observation. I have downloaded the .antab files, which

contain system temperature values for the antennas, from the observation page for HartRAO(HH), Mopra(MP) and Parkes(PA). After some editing the files are loaded in to AIPS separately.

Sometimes the observing log in the VLBI observation may not contain system temperature information for the participating antennas. If there are not any T_{sys} measurements, like in the case of AK, AT, CD and HO in our observation, we use nominal values for each antenna. Therefore, I have created a file using the nominal values for AK, AT, CD and HO together.

TABLE 4.3: Nominal SEFD at 1.6 GHz

Antennas	SEFD(Jy)
ASKAP	6000
ATCA (single 22m dish)†	340
Ceduna	800
Hobart	420

† For n number of dishes used, the SEFD will be $\frac{340}{n}$.

4.2.2 Amplitude calibration

The main calibration process involves phase and amplitude calibration. The observed visibility amplitude is affected by factors such as aperture efficiency, atmospheric absorption and pointing errors as mentioned in the previous chapter. Amplitude calibration involves finding amplitude gains so as to remove or minimize the effect of the factors, mentioned above, on the amplitude. The calibration steps described in this section use a priori information about the performance of the antennas. After getting the T_{sys} and the antenna gain information I run ACCOR, this corrects the amplitude in cross correlation spectra due to errors in parameters of samplers using measurements of auto-correlation spectra. The effect of running ACCOR can be seen by looking at the auto correlation amplitude before and after ACCOR.

After calculating the gains from the T_{sys} values, I found very high gain in Hobart antenna between 1/22:30:00 - 1/23:03:00 (the first number represents day relative to the day that the observations started, which is the first day and the other numbers represent the UTC time in that day). Some of the values are approximately three times

higher than that of the average one, as a result of this the data at this time are likely poor, so it is removed (flagged). Similarly, for AK, the T_{sys} value and gain amplitudes suddenly increased at about 2/9:22:00 to 2/9:26:00, but not as bad as the HO ones in terms of fraction of average gain. I also found few high points in different baselines and I removed these points using the AIPS task IBLED, which is used to edit visibility data interactively.

Plot of visibility amplitude vs frequency, using AIPS task POSSM, showed cross-polarization (RL or LR) flux density higher than the parallel polarization (LL or RR) flux density for AK baselines and PA baselines. This is a diagnostic to tell the right and left polarization was flip either during the observation or correlation, and the right circular polarization (RCP) recorded as left circular polarization (LCP) and vice versa. The polarization is then corrected for the visibilities involving either AK or PA, using SWPOL task, which swaps the polarization in a uv data base.

4.2.3 Phase calibration

In this subsection we first discuss how to find the single-band delays. What we want to do is to calibrate out the relative phase and delay between the four IFs, this enables us to coherently average over the four IFs when ever needed. The relative phase and delay is usually pretty constant so the approach is just to solve for the delay using AIPS task FRING for one scan only. This task determines the residual group delay and delay rate in the visibility data. Therefore, what we need is one scan, preferably where all the antennas observed a particularly strong source. I have used Mopra as a reference antenna because it has more data than the other antennas.

I chose 0454-810, which was observed by all 7 antennas and for which the signal was strong. Then, the next step is to run FRING. I have five scans of the source 0454-810, but I picked the one at 01/14:15:52 - 01/14:20:20. The resulting SN table, which contains the solution after running FRING, has entries for one scan, and therefore one source. The solution is extrapolated for other sources. Figures 4.2 and 4.3 show the effect of single band delay calibration. At this stage we expect the phases to be aligned up across all IF's, so that the visibility phase is a continuous, linear function of frequency. The first channel from IF 1 and 3, and the last channel from IF 2 and 4 are flagged due to extremely low amplitude. This is shown in the two figures below(Figure 4.2 and 4.3), there are no points in these channels.

A phase of -180 is equal to +180, so having phase points at the very top and bottom means the points are close to each other. The scattered points in the AK-HO baseline show that the signal is noisy in this baseline.

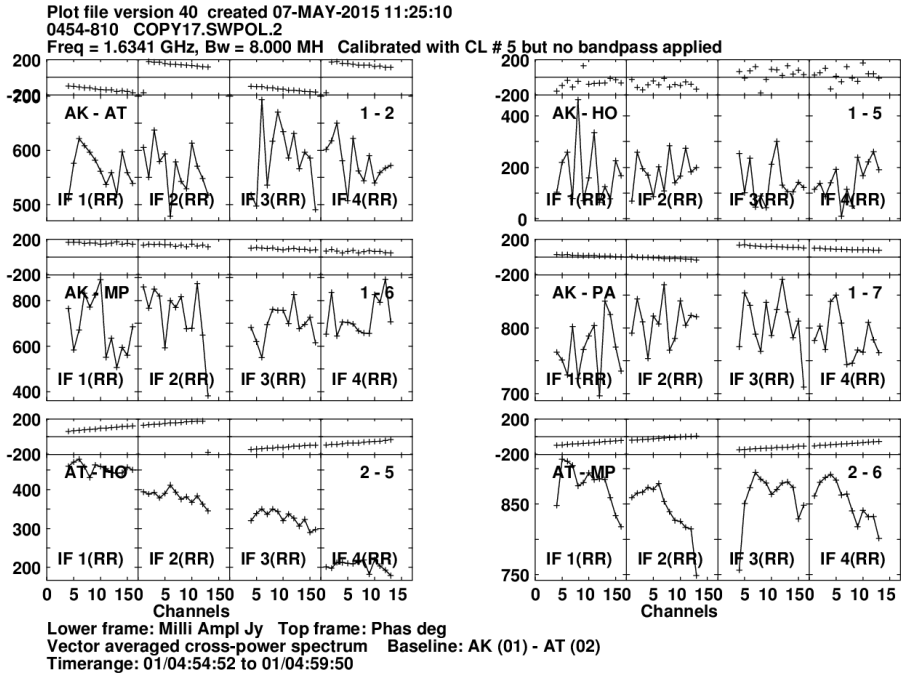

FIGURE 4.2: The top panel in each image shows the visibility phase, and the bottom panel shows the visibility amplitude, both as function of channel for different baselines before single band delay calibration. AK(1)– ASKAP, AT(2)–ATCA, CD(3)–Ceduna, HH(4)–HartRAO, HO(5)–Hobart, MP(6)–Mopra and PA(7)–Parkes

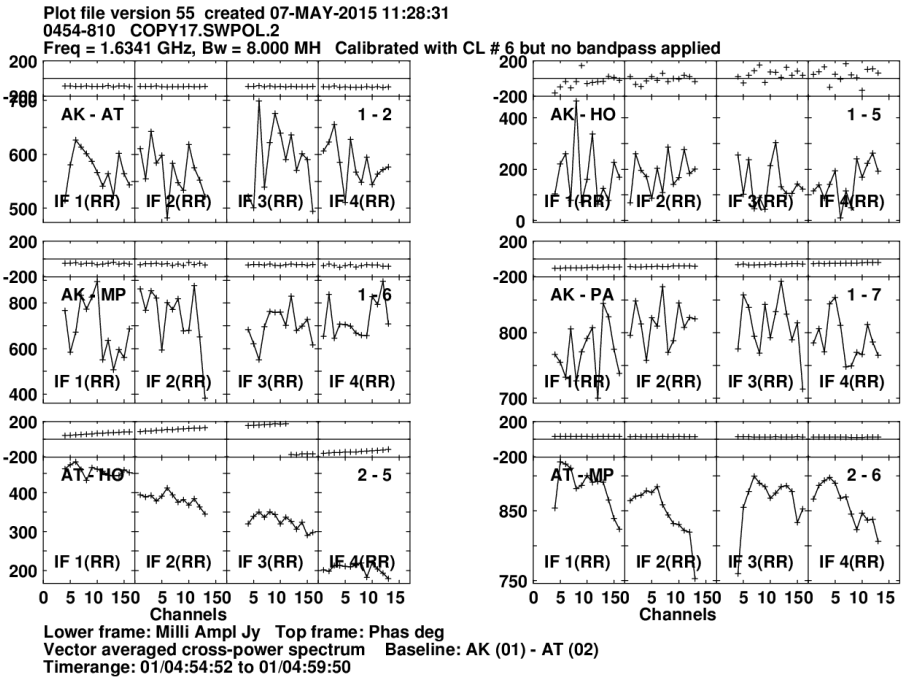

FIGURE 4.3: The top panel in each image shows the phase vs channel and the bottom panel shows amplitude vs frequency for different baselines after single band delay calibration. AK(1)– ASKAP, AT(2)–ATCA, CD(3)–Ceduna, HH(4)–HartRAO, HO(5)–Hobart, MP(6)–Mopra and PA(7)–Parkes

The second part of phase calibration requires running multi-band FRING. In this case we need to obtain a solution for each source rather than using one source to get a solution and extrapolating for other sources as we did for single band delay. The multi-band FRING should produce an SN table with rates and delay solutions for every antenna for every scan that we have observation. It will likely fail on a number of solutions because some antennas didn't observe, or since we are using a point-source model, which might not fit well if the sources are heavily resolved, and therefore cause those solutions to fail. In the single band delay we have calibrated the relative phase and delay between IFs, and here from multi-band FRING we want to get solutions for residual delays and rates by combining the four IFs.

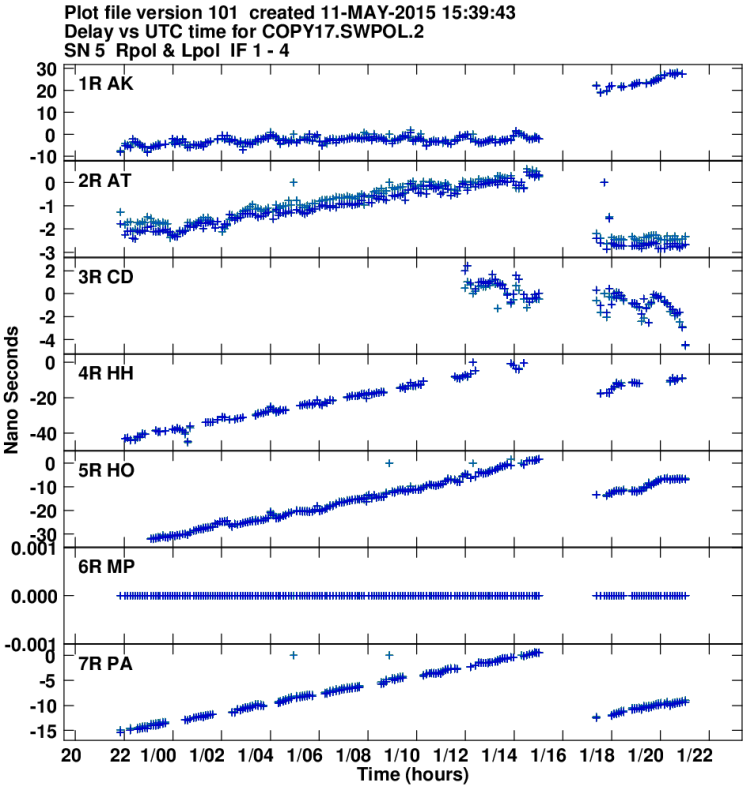

FIGURE 4.4: Residual delay solution obtained from multi-band FRING.

It is important to know and correct the phase shift due to delay and rate, because at the end we may want to coherently average the visibility over both time and frequency. In order to do this averaging we need the phase to remain (nearly) constant over the averaging interval. Ideally the phase shift in the averaging interval is less than 1 radian. The resulting SN table shows that the residual delay is less than 40 nanosecond for HH, less than 30 nanosecond for HO and less than 15 nanosecond for the other antennas (Figure 4.4). These delays results maximum of 2, 1.5 and 0.5 radian phase shift over our 8MHz observing band width respectively. Most of the time the delay rate is below 20

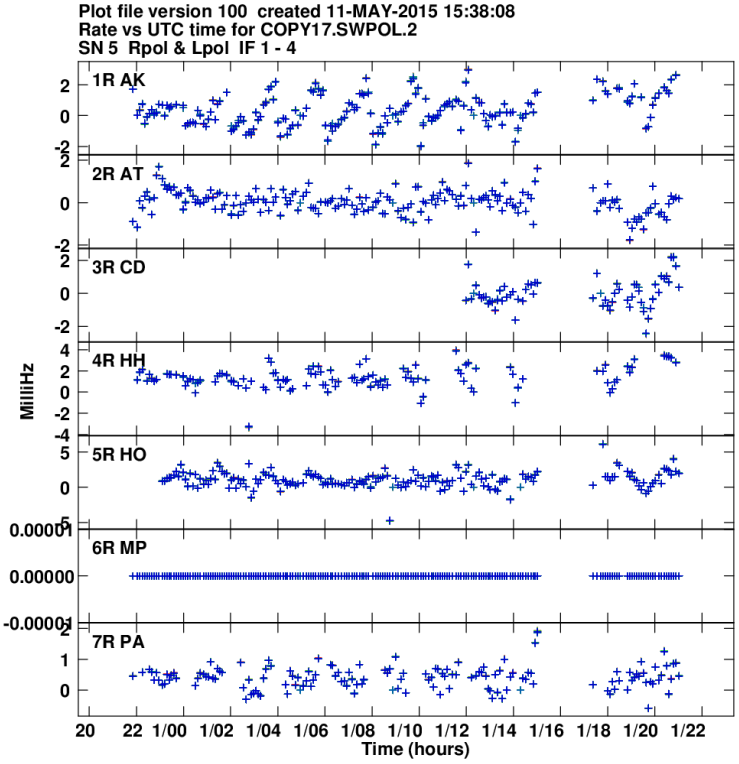

FIGURE 4.5: Delay rate solution obtained from multi-band FRING.

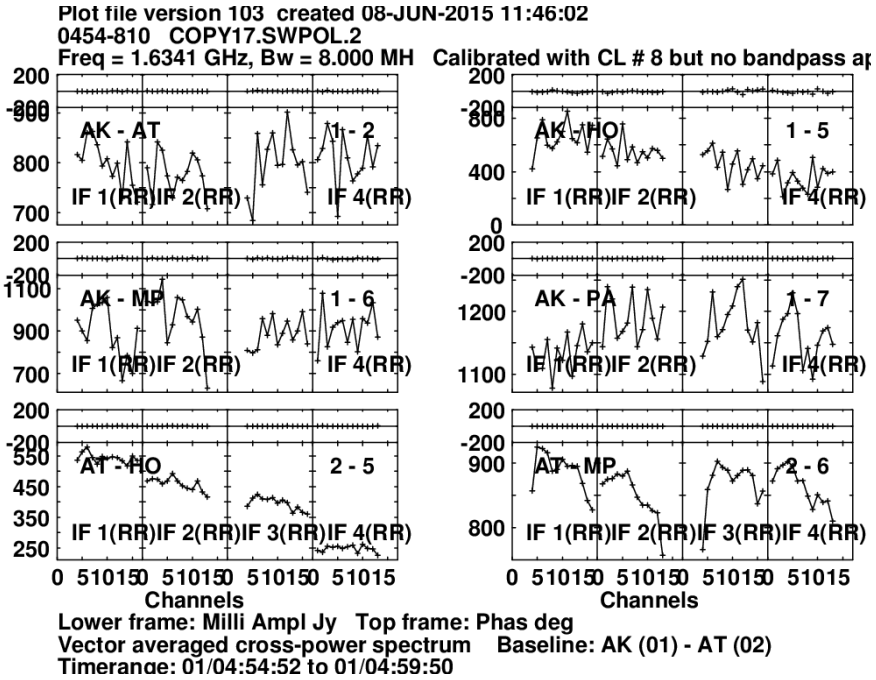

FIGURE 4.6: The top panel in each image shows the visibility phase vs channel and the bottom panel shows amplitude vs frequency for different baselines after multi-band delay calibration. The visibility phase lined up close to zero after applying multi-band FRING's solutions to the data. AK(1)– ASKAP, AT(2)–ATCA, CD(3)–Ceduna, HH(4)–HartRAO, HO(5)–Hobart, MP(6)–Mopra and PA(7)–Parkes

milli-Hz (Figure 4.5) and the corresponding phase shift is less than 1 radian. Therefore, we are safe to average the visibilities over our observing band without significantly affecting the result. It is also reasonable to average over the scan time since the delay rate is close to zero.

After getting the rate and delay solutions, the solution was edited, smoothed and finally applied to the existing CL table.

4.2.4 Additional calibration

After multi band FRING I wanted to check if we need further amplitude and phase calibration. I took sample sources to see if there is any change in the images after further amplitude and/or phase self calibration. I first determined the gain for each antenna, as I will describe below, using 6 relatively strong sources observed by all antennas, to check if the amplitude gains are about right or not, and then fix the ones that are not.

UVFIT is a task in AIPS to fit a model consisting of elliptical Gaussian, uniform spheres to a uv data file. I first ran UVFIT to get the idea of the total flux density by fitting the model, then by fixing the total flux density I rerun UVFIT to fit the antenna gain factors as well as the model. The aim was to see whether any particular antenna always came up with low or high gains. The result of the UVFIT shows that antenna PA always got a low gain(by $\sim$ 15 percent or so), and antennae CD and HO always got a high gain by 48 and 29 percent respectively, while the others with close to 1.

Therefore, I run UVFIT again to estimate the total flux density of each of the six sources, and then rerun UVFIT, using the estimated total flux density, to get the antenna gain corrections for each antenna. Then I averaged the gain correction for the different sources together to come up with a single value for each antenna gain correction. The results are shown in Table 4.4.

The amplitude part of the gain is not much affected by the atmosphere (typically atmospheric opacity at L-band is very low and the atmospheric transmission at L-band is probably more than 90 percent, so the contribution to the gain from the atmosphere will be less than 10 percent) (Thompson, 1971; Rohlfs & Wilson, 2004). So pointing at different parts of the sky or changes with time in the atmosphere should only have a relatively minor effect on the gain amplitude. Therefore, the antenna gain problem is probably due to the antenna itself.

I made corrections only for antennas (CD and PA only) with small gain correction uncertainty and with the mean gain corrections greater than $(1 + \delta)$, where δ is the

TABLE 4.4: Mean and rms of antenna gain corrections for six selected sources

Antennas	Mean	rms(standard deviation)
ASKAP	1.04	0.23
ATCA	1.03	0.02
Ceduna	1.48	0.10
HartRAO	1.04	0.20
Hobart	1.29	0.15
Mopra	0.98	0.02
Parkes	0.74	0.03

standard deviation of the gain corrections. The gain correction for AT is very small (i.e near 1.0), therefore, I didn't apply the correction.

4.3 Imaging

After the final calibration I did the imaging (i.e inverse Fourier transform of calibrated visibility data) using the same software (AIPS) that I used for the data reduction. The resulting inverse Fourier transform of the sampled visibility is the convolution of the true intensity distribution and the synthesized beam (see equation 2.21). To recover the true intensity distribution we used a deconvolution algorithm called CLEAN, which involves subtraction of the clean(CLEAN) component model (i.e model image using the brightest point in the image) from the data in a number of iterations or cleaning. The sum of the flux density of these CLEAN components is called the total CLEANed flux density. In Table 4.5, I give the total CLEANed flux densities for each of the sources I imaged. The other image parameters, the peak brightness and the image off-source rms brightness are also given in that table. The off-source rms brightness is usually due to thermal noise, residual calibration error and bad data. The effect of calibration errors in the image is mostly multiplicative therefore even the small calibration error could result in higher off-source rms brightness depending on how strong the source is. The off-source rms brightness also depends on the scan time, band width and the number and type of telescopes involved.

TABLE 4.5: Image parameters: Column 1 gives the sources name, column 2 gives the peak brightness, column 3 gives the off-source rms brightness and column 4 the total CLEANed flux density

Sources	+ve Peak brightness (Jy/beam)	off-source rms brightness (mJy/beam)	CLEANed flux density (mJy)
0056-572	361	6.3	369
0252-549	678	16.1	687
0312-770	486	9.6	498
0334-546	260	5.5	281
0454-810	686	11.2	706
0530-727	423	14.1	429
0743-673	841	20.4	898
0903-573	251	3.7	252
1036-529	440	7.5	496
1039-474	891	13.2	974
1049-534	841	15.4	905
1059-631	566	9.4	735
1105-680	502	10.0	521
1109-567	381	2.5	539
1129-580	469	4.5	491
1143-696	274	4.4	279
1148-671	914	18.0	1080
1204-613	134	2.2	232
1249-673	430	4.3	298
1251-713	470	10.5	487
1312-533	178	3.0	218
1352-632	285	17.6	728
1420-679	712	13.2	752
1424-418	2000	2.3	2252
1509-564	238	7.9	418

TABLE 4.5: Continued

Sources	+ve Peak brightness (Jy/beam)	off-source rms brightness (mJy/beam)	CLEANed flux density (mJy)
1511-558	830	18.3	1020
1619-680	1030	17.8	1060
1624-617	367	5.2	400
1659-621	467	5.2	566
1740-517	2720	4.9	3650
1758-651	469	6.2	489
1806-458	226	4.1	263
1831-711	723	13.9	755
1903-802	536	16.2	550
1925-610	527	9.9	660
1935-692	795	13.4	830
2030-689	118	2.4	121
2059-786	260	5.2	265
2142-758	755	12.1	768
2146-783	496	5.3	509
2300-683	456	7.4	468
2333-528	1190	19.8	1250
2353-683	482	9.4	522

The image dynamic range which tells us about the image quality is the ratio of the peak brightness to the off-source rms brightness. The distribution of the dynamic range is shown in Figure 4.8. The mean value is 60 with a median of 58. This is sufficient to study the compactness of the source because we are not that interested in every little detail about these sources we only want to look how much of the total flux density is concentrated at the central component, we mostly just want to know whether they will make good calibrators.

The average off-source rms brightness level in the image is 9.6 mJy/beam with a median off-source rms brightness of $\sim$ 9.4 mJy/beam. The values of the peak brightness range from 118 mJy/beam to 2720 mJy/beam with mean peak brightness of 649.9 mJy/beam and median 499 mJy/beam. All except two sources have peak brightnesses greater than 200 mJy/beam. The average radius of the convolving beam (by assuming a circular beam area with radius equal to (Convolving beam size/4)$^{0.5}$) of the observation

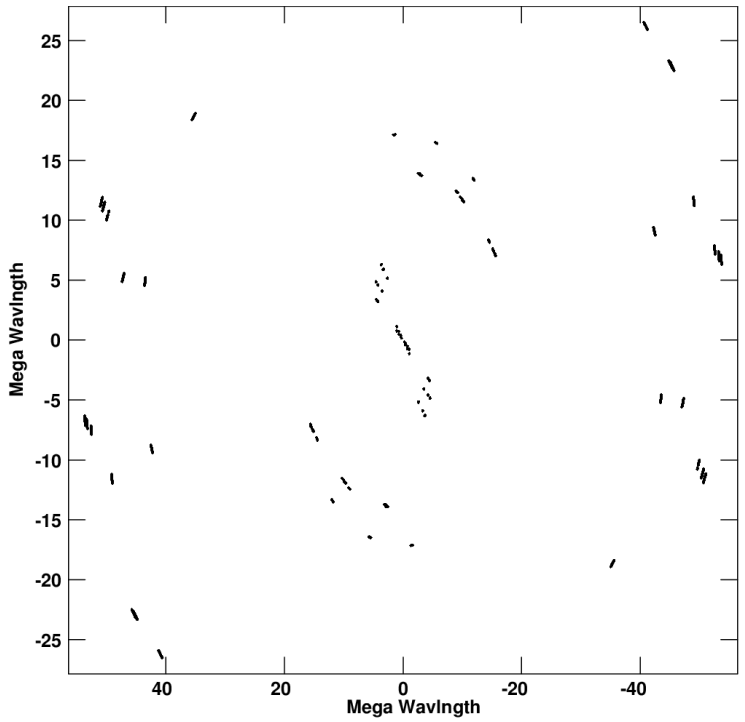

FIGURE 4.7: UV coverage for 1806-458: The uv coverage for this source is relatively bad, which could affect our image.

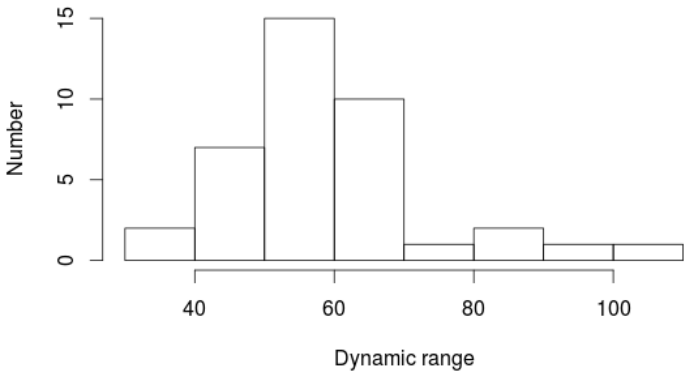

FIGURE 4.8: Dynamic range distribution of the sources

is 2.7 milliarcsecond with minimum and maximum equal to 1.7 and 4.3 milli-arcsecond respectively.

Chapter 5

Results and Discussion

This chapter discusses the results I obtained, and my determination of which of our sources are suitable calibrators at 1.6 GHz observation by characterizing the compactness and brightness of the sources. I also examine how the properties of some of the selected sources at 1.6 GHz relate to those seen at 8.4 GHz.

5.1 Compactness of the sources

In this section I want to determine the compactness of the sources. Even though it is difficult to get ideal calibrator sources we can get sources which are compact and bright enough to be used as a calibrators. To compute the brightness of the sources is straightforward. What is more difficult to determine is the compactness of the sources. The relative compactness of a source can be measured in different ways and we determine the source's suitability as a calibrator by combining information obtained from four different measures of source compactness, which will be discussed in the next sub-sections.

5.1.1 Core fraction

The core fraction C of a source is the ratio of the core flux density to the total flux density. I define the core flux density as the sum of the CLEANed flux density within angular radius of 2.5 milliarcsecond from the brightest pixel and the total flux density is defined as the sum of the flux density of all CLEAN components. The angular radius of 2.5 milliarcsecond is a representative of the synthesized beam size obtained using global VLBI with a baseline length of 10,000 km. This baseline length is close

to the longest baseline we have in our observation and we want to see how compact our sources are even for global VLBI observations. Since CLEAN components can be both positive and negative the core fraction can exceed unity. The values of the core fractions for the sources are listed in Table 5.1. The distribution of the core fraction for our sources is shown in Figure 5.1. The average core fraction is 0.85 and the median is 1.00. This shows that most of our sources are largely dominated by the core or most of the flux densities are concentrated in the central component of the sources.

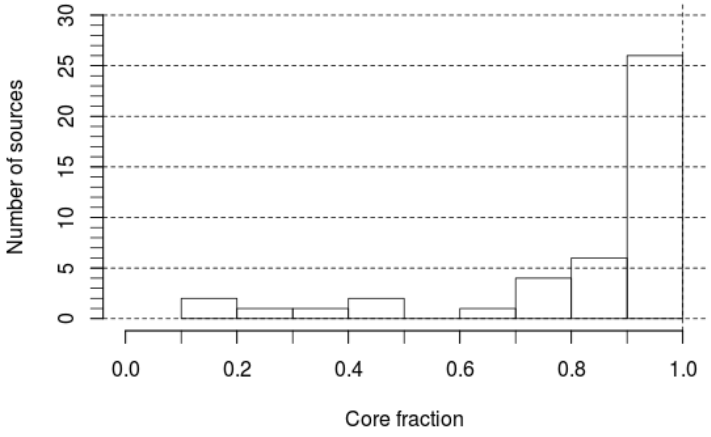

FIGURE 5.1: Core fraction distribution of the sources

5.1.2 Radial extent

I calculated two types of radial extent of the sources, which give us different information about our sources. The first one is the flux density weighted radial extent of the sources, which is given by

$$r_{wt} = \frac{\sum_i S_i r_i}{\sum_i S_i} \tag{5.1}$$

where r_i is the radius of the i^{th} CLEAN component from the brightest point, and S_i its flux density. Figure 5.2 shows the distribution of the flux density radial extent r_{wt} of the sources. The flux density weighted radial extent of the sources ranges from 0.41 to 5.36 milliarcsecond with mean of 1.57 milliarcsecond and median 1.21 milliarcsecond. The r_{wt} of the sources are given in Table 5.1.

The other type of radial extent measurement, which is the 95 percent flux density radius, $r_{95\%}$, is also measured from the brightest point. $r_{95\%}$ is a radius with in

which 95 percent of the flux density of the source is contained. The way I determined $r_{95\%}$ is just by adding the flux densities of the CLEAN components starting from the brightest point up to some radius until I get 95 percent of the total CLEANed flux density. The $r_{95\%}$ of the sources are given in Table 5.1.

Figure 5.3 shows the distribution of the 95 percent flux density radius of the sources ranging from 0.82 to 16.89 milliarcsecond with mean and median equal to 4.13 and 2.53 milliarcsecond respectively.

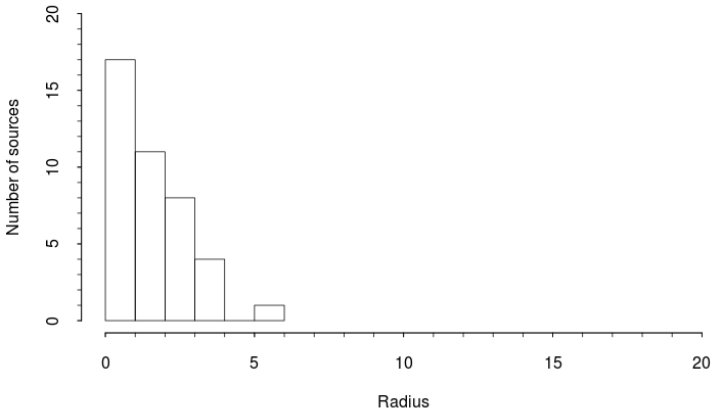

FIGURE 5.2: Distribution of r_{wt}, which is given in milliarcsecond

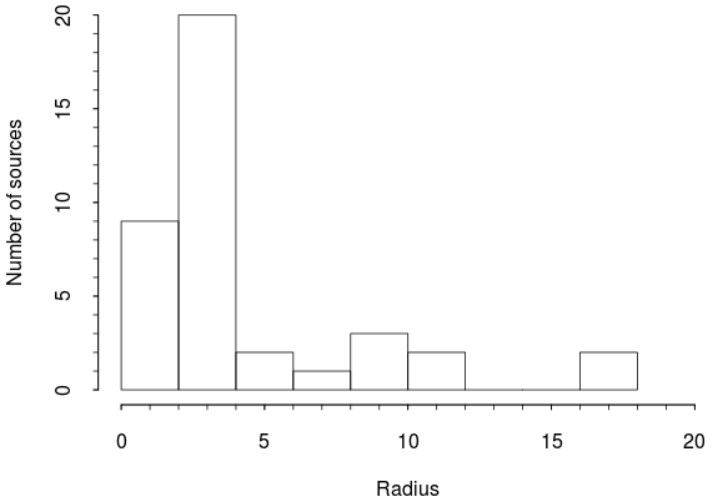

FIGURE 5.3: Distribution of the 95 percent flux density radius. The radius is given in milliarcsecond

5.1.3 Flux density variation with uv-distance

As I mentioned earlier, the correlated flux density or the visibility amplitude of an unresolved source is constant with baseline length or uv-distance, but for resolved sources the correlated flux density depends on the projection of the baseline vector on the source plane (uv-plane) and on its orientation. In this section I examine how much the correlated flux density of our sources falls off with uv-distance.

The visibility plane is the Fourier transform of the image plane and the correlated flux density fall off is related to the radius of the source. Therefore, I will discuss the correlated flux density fall off in terms of the brightness variation with radius of the source in the image plane to make the comparison with other metrics, which I calculated in section 5.1.2, easier as all will be in the same units.

I will determine the angular radius at which the average brightness is half the maximum one. Determination of the angular radius will give us some complimentary information about our sources if they are unresolved or not, and then I will use it with the other parameters I got for the sources to determine the relative quality of our sources to use as a calibrator.

To estimate the angular radius, we first fit a circular Gaussian model to the visibilities, then take the half width at half maximum (HWHM) of the circular Gaussian fitted to the visibilities. The HWHM of the sources ranges from 0.3 mas to 12.8 mas, with mean and median equal to 2.19 and 1.1 mas respectively (see Table 5.1). The HWHM distribution of the sources is shown in Figure 5.4.

TABLE 5.1: Weighted radial extent (r_{wt}), 95% flux density point radius (r_{95}), Half width at half maximum (HWHM) and core fraction (C) of the sources

Sources	r_{wt}(mas)	$r_{95\%}$(mas)	HWHM(mas)	C
0056-572	0.65	1.01	0.55	1.00
0252-549	0.52	1.28	0.75	1.00
0312-770	0.85	2.64	1.00	0.91
0334-546	1.04	1.63	1.15	1.00
0454-810	0.57	4.12	0.30	0.90
0530-727	0.46	1.15	0.50	1.00
0743-673	1.73	2.07	1.58	1.00
0903-573	0.62	2.17	0.50	0.96
1036-529	3.01	8.21	1.35	0.69
1039-474	1.78	2.30	1.55	1.00
1049-534	3.25	11.05	1.35	0.76
1059-631	2.94	2.97	5.73	0.50
1105-680	1.70	2.42	1.05	1.00
1109-567	5.23	5.60	6.90	0.34
1129-580	1.09	2.90	1.35	0.93
1143-696	0.41	2.53	0.50	0.85
1148-671	3.03	10.93	1.30	0.86
1204-613	11.62	23.29	10.30	0.30
1249-673	1.30	2.88	1.35	1.00

TABLE 5.1: Continued

Sources	r_{wt}(mas)	$r_{95\%}$(mas)	HWHM(mas)	C
1251-713	0.64	2.30	1.15	0.89
1312-533	2.18	6.98	1.15	0.80
1352-632	18.53	26.58	12.80	0.13
1420-679	1.62	5.39	1.10	0.85
1424-418	2.26	8.77	0.65	0.75
1509-564	11.49	15.49	11.90	0.16
1511-558	2.85	3.01	5.15	1.00
1619-680	3.19	9.83	0.75	0.78
1624-617	0.99	2.86	1.00	1.00
1659-621	2.46	3.29	1.30	0.92
1740-517	5.36	16.89	5.65	0.43
1758-651	0.48	1.81	0.65	1.09
1806-458	2.22	3.55	1.20	1.00
1831-711	1.00	2.57	0.90	1.00
1903-802	0.83	2.09	0.99	1.00
1925-610	1.15	16.12	0.90	0.88
1935-692	1.21	2.01	1.40	1.00
2030-689	0.59	0.89	0.80	1.00
2059-786	1.27	2.49	1.00	1.00
2142-758	0.93	1.25	1.00	1.00
2146-783	0.78	1.61	0.90	1.00
2300-683	0.57	0.82	0.45	1.00
2333-528	0.97	2.01	0.85	1.00
2353-683	1.23	2.06	1.35	1.00

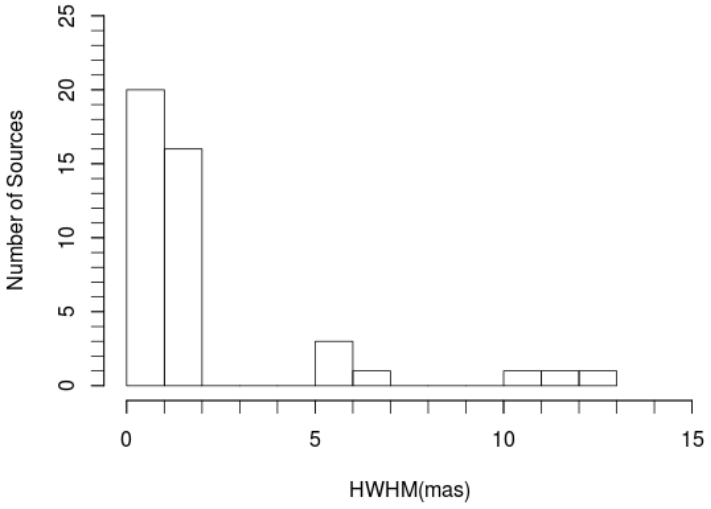

FIGURE 5.4: Distribution of the HWHM. The HWHM is given in milliarcsecond (mas)

5.1.4 Images

In this section we present images of our sources. The contour plots of our sources are shown in Figure 5.5. The convolving beam size for each source is shown at the top right corner of the images. The convolving beam sizes differ for different sources as the maximum baseline is different for different sources. Comparing the convolving beam size and the 50 percent level contour plot of a source is the other way of checking how resolved an image is.

The size and shape of the 50 percent contour of 39 of the sources is approximately equal to those of the convolving beam size, suggesting that most of the flux density of the sources is contained within the convolving beam for each sources. All the 39 sources consist of a single compact component except 1740-517, which contains a second faint component. For 1109-567, 1509-564, 1204-613 and 1352-632 we see the size of their 50 percent contour is larger than the convolving beam size. These four sources have extended regions that are clearly visible in the contour plot.

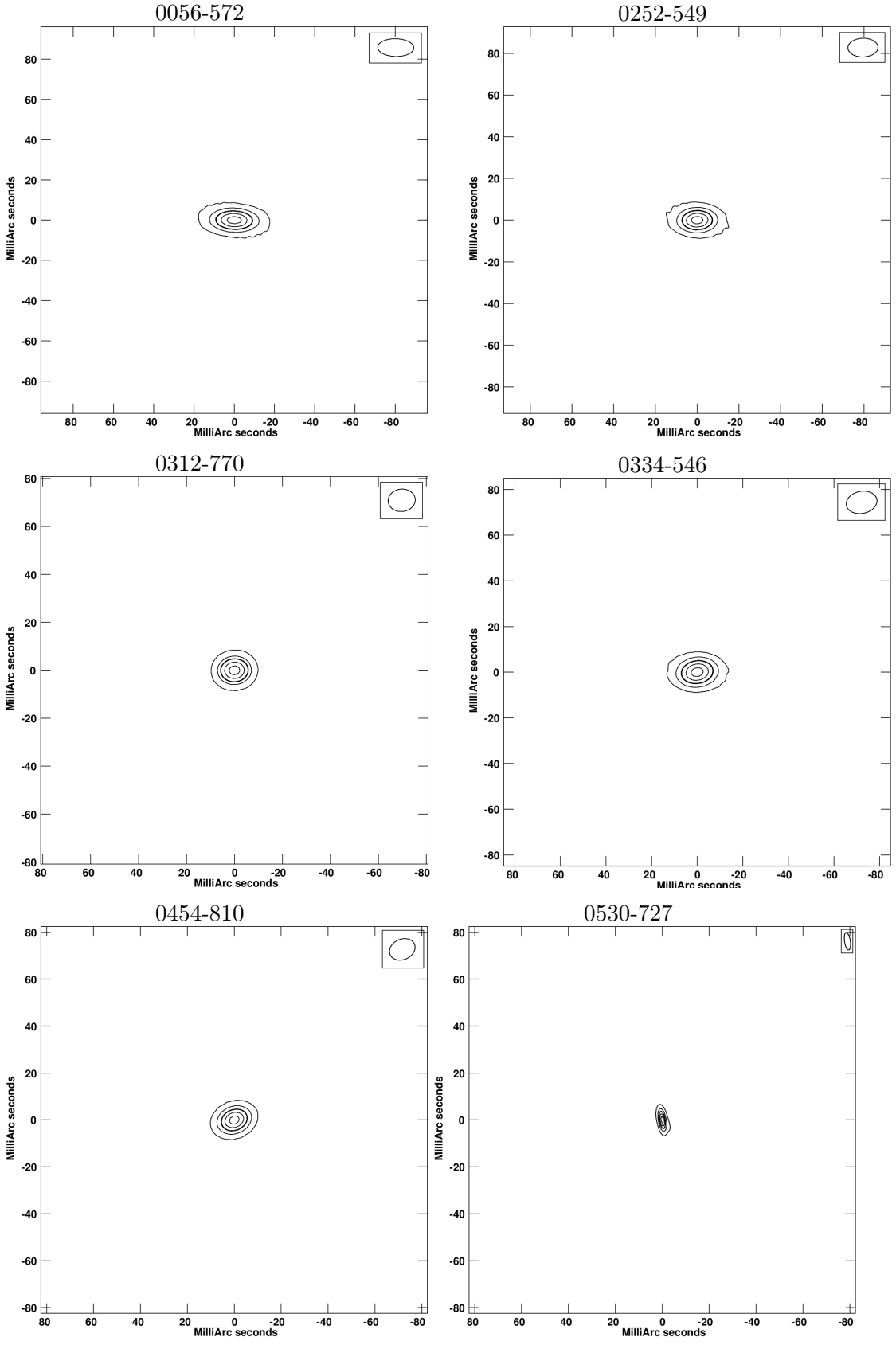

FIGURE 5.5: Contour plots of the sources. The contours are drawn at 10, 30, 50,70 and 90 percent of the peak brightness with the 50 percent contour being darker than the rest. The FWHM of the convolving beam is shown in the upper right in each panel.

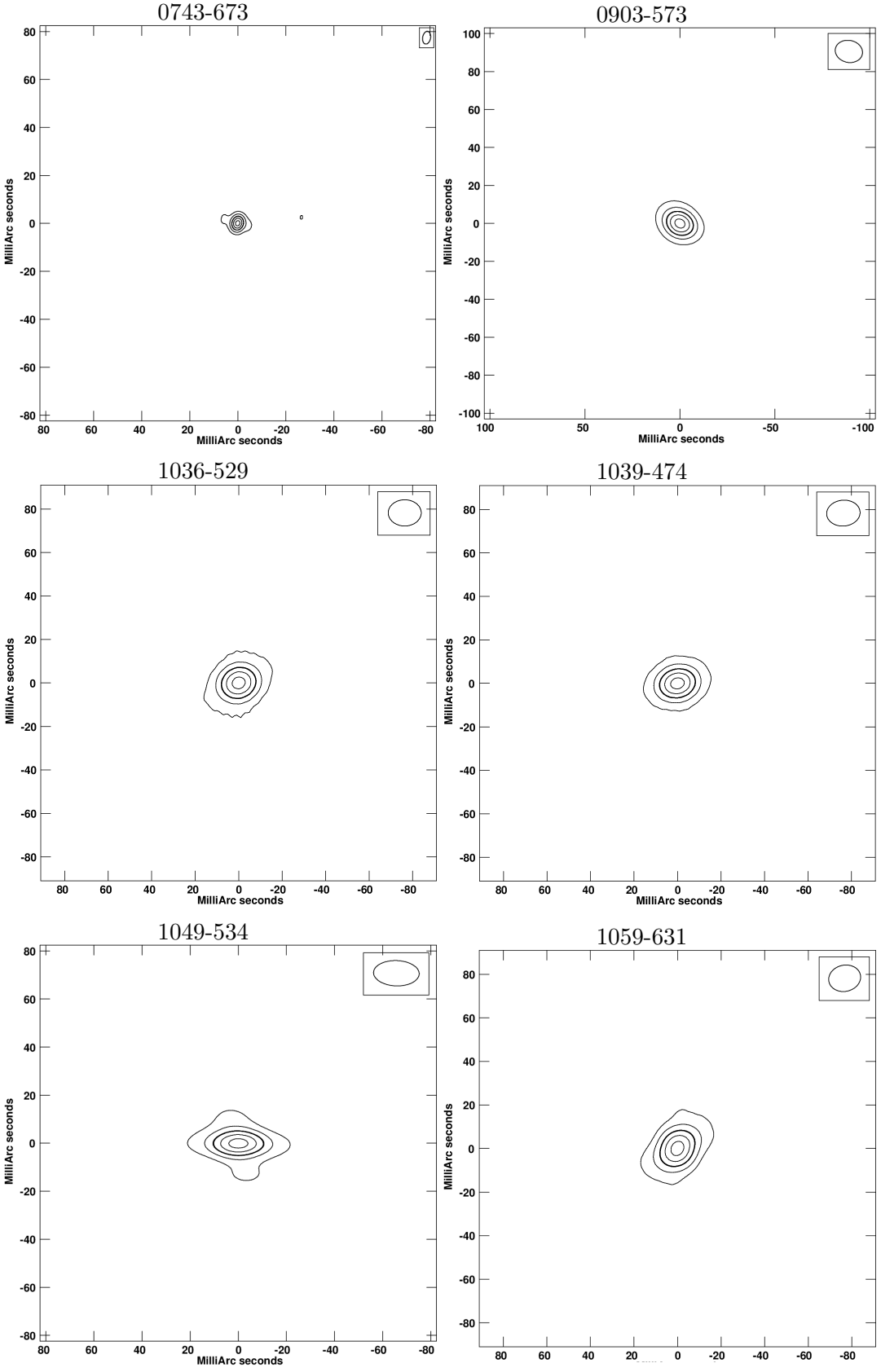

FIGURE 5.5: Continued

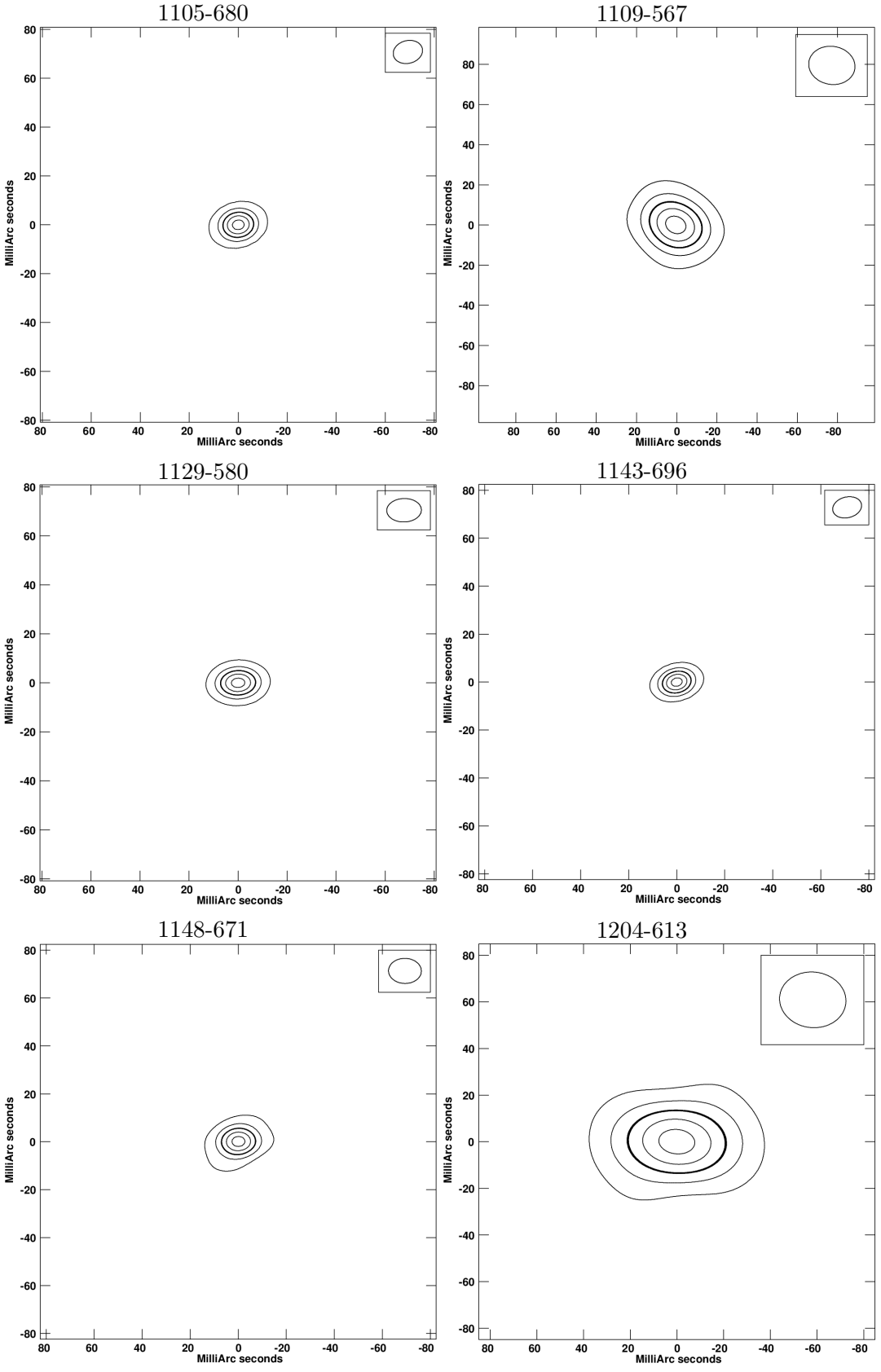

FIGURE 5.5: Continued

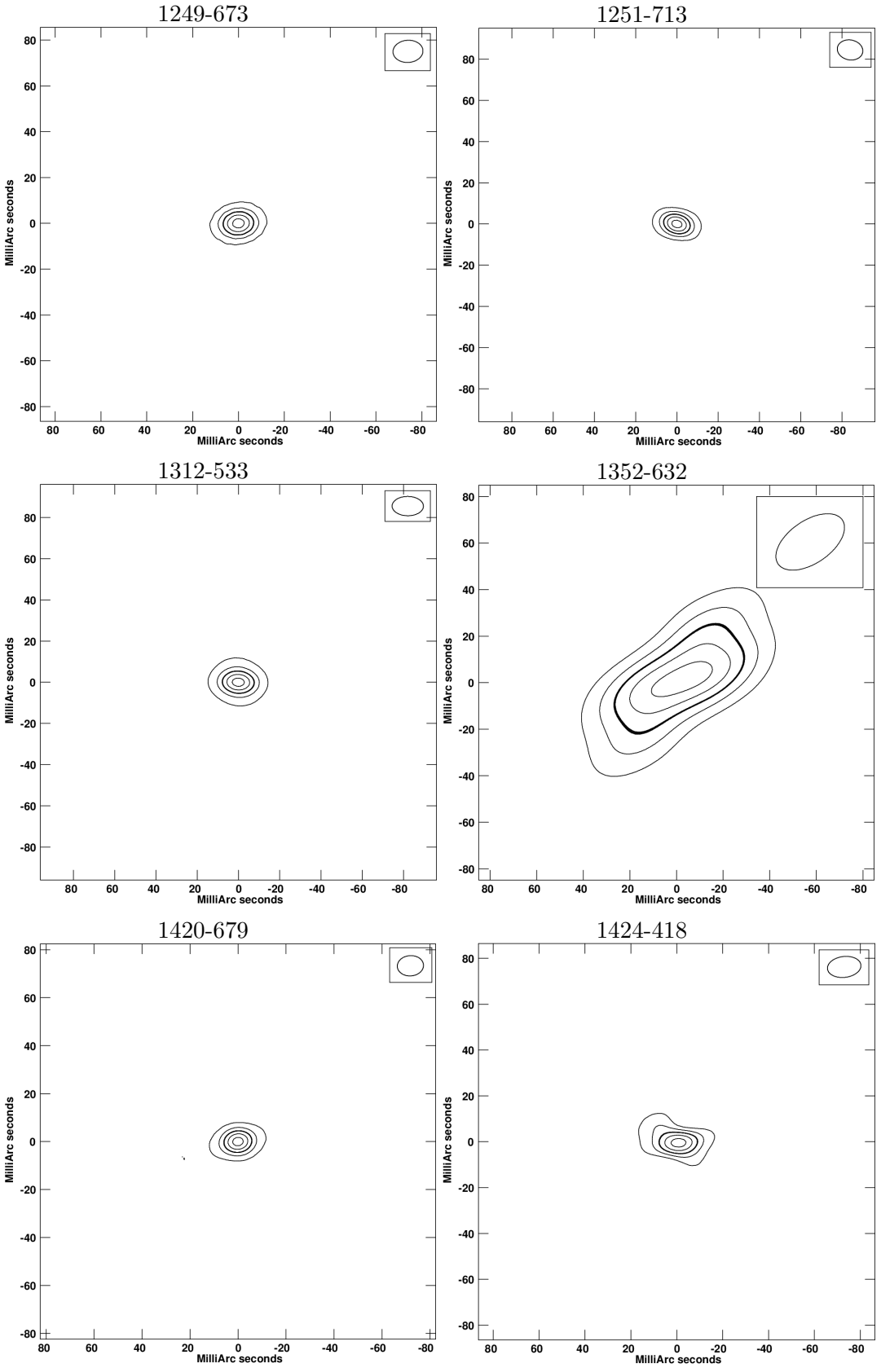

FIGURE 5.5: Continued

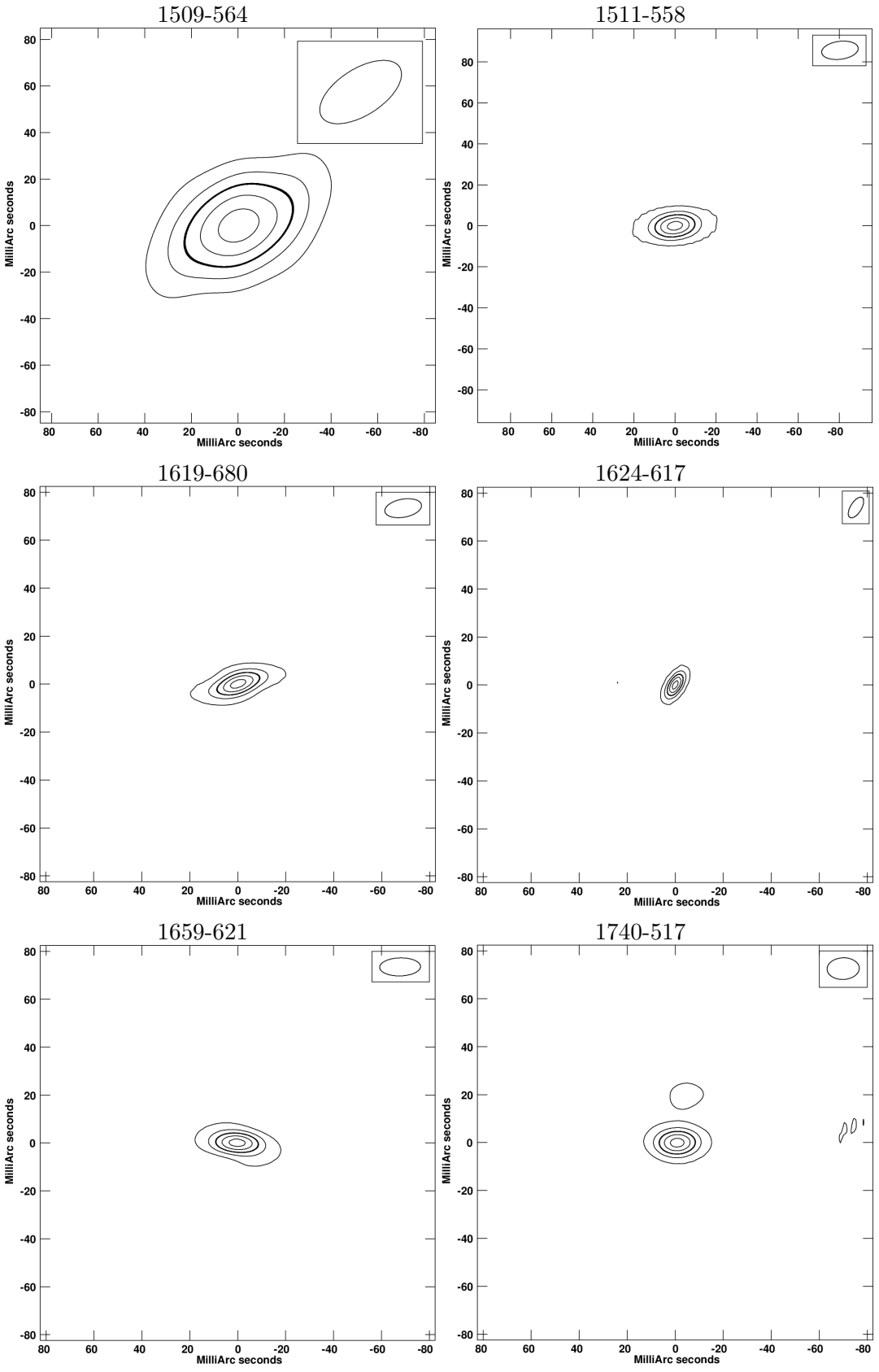

FIGURE 5.5: Continued

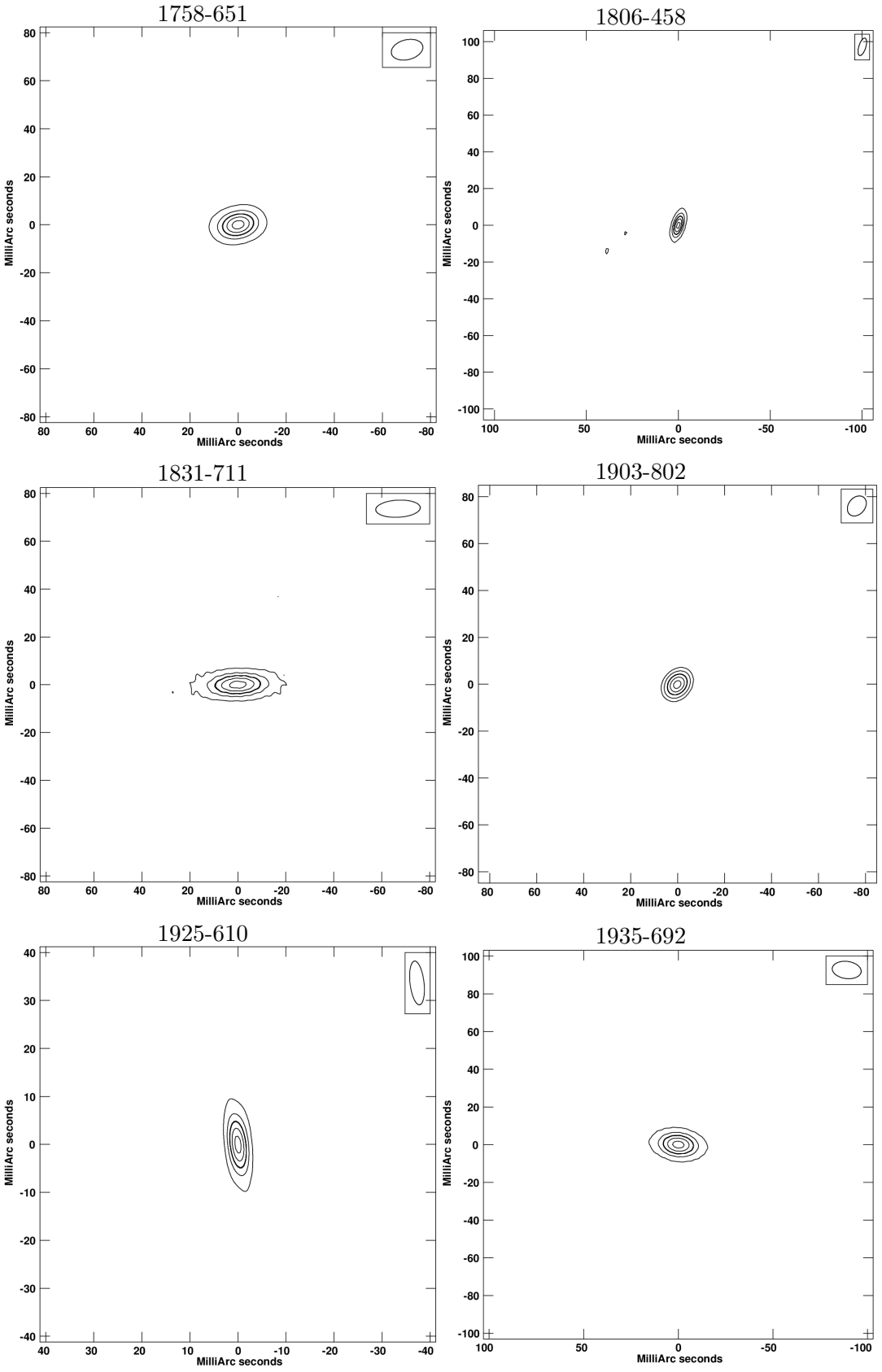

FIGURE 5.5: Continued

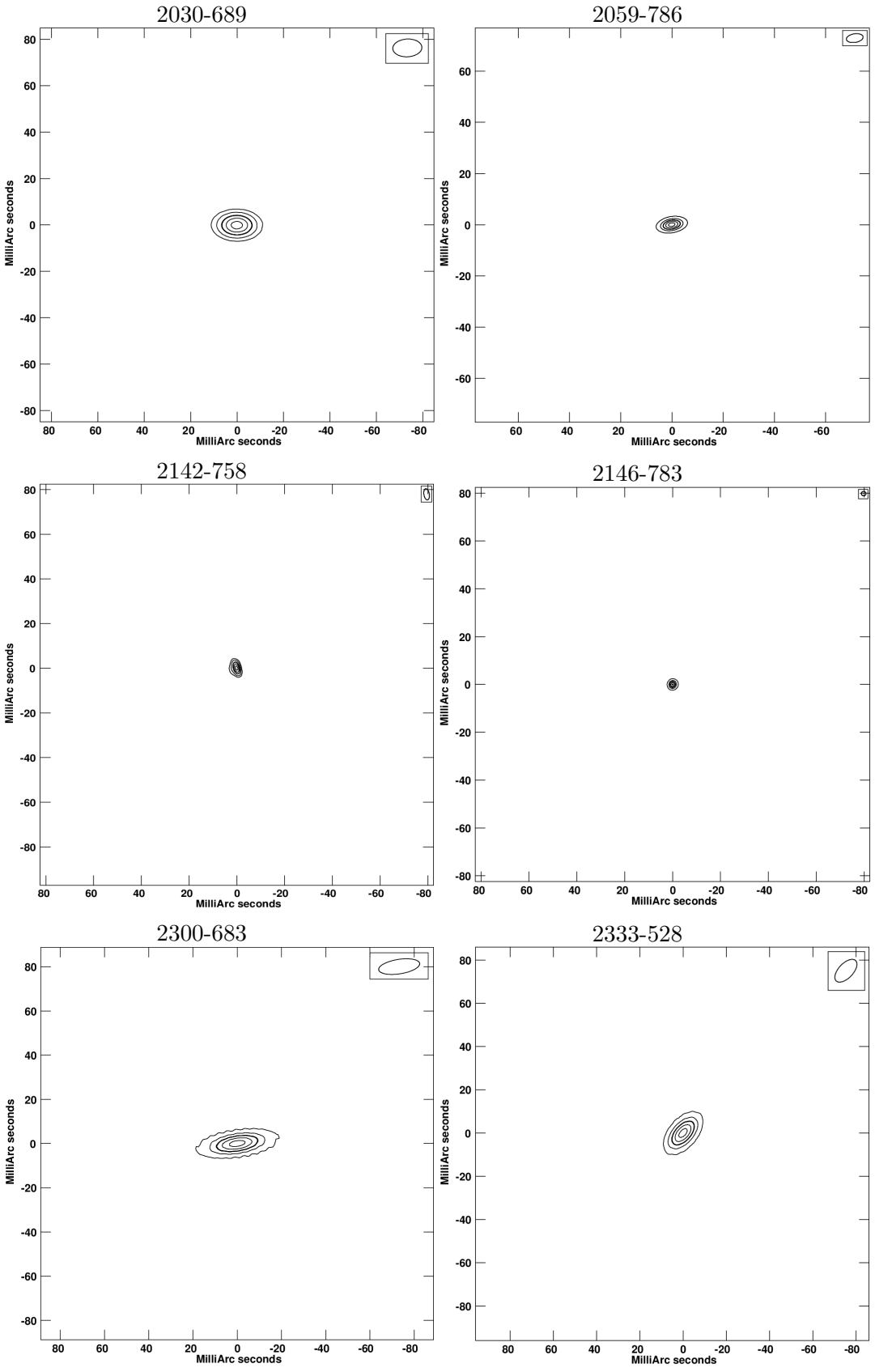

FIGURE 5.5: Continued

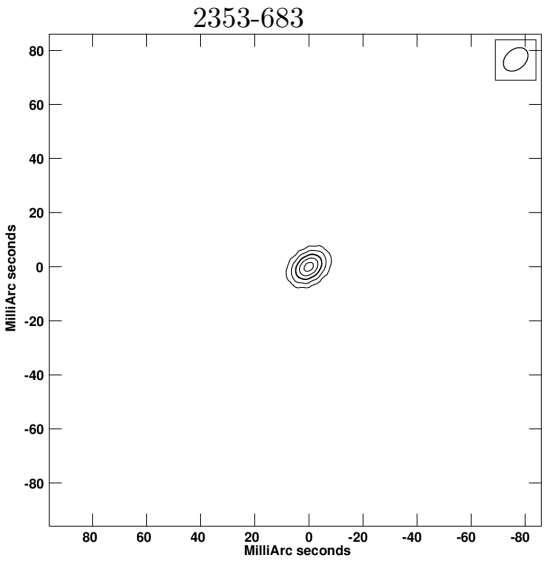

FIGURE 5.5: Continued

5.2 Classification of Calibrator Quality

To determine whether my sources are suitable as calibrators at 1.6 GHz I have developed a set of complimentary metrics, which are described in section 5.1. I averaged the three radial measurements: the weighted radial extent, the 95 percent flux density radius and the 50 percent point flux density radius for each sources to get the average radius r_{av}. The values of the average radius of the sources are given in Table 5.2. The distribution of the average radius is shown in Figure 5.6. The classification of calibrator quality I do here is mainly based on the average radius and the core fraction of the sources.

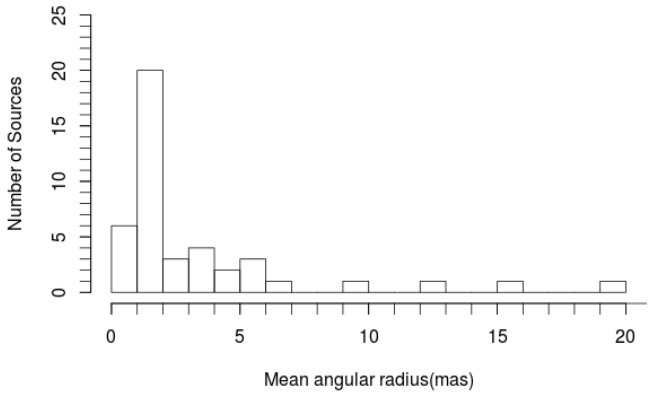

FIGURE 5.6: Distribution of the average radius r_{av} for our sources

We divided our sources into four groups according to their compactness and brightness, as follows:

- **Very Good**:- contains sources with core fraction C $\geq$ 0.8 and average radius r_{av} $\leq$0.4 mas. All sources in this group have sufficient flux density (good signal to noise ratio) on all baselines.
- **Good**: contains sources which are not in the first group but which have C$\geq$ 0.5 and $r_{av} \leq 6$ mas. They also have sufficient flux density (good signal to noise ratio) in all baselines.
- **Intermediate**: contains sources which are not in the first or the second group but which have C$\geq$ 0.5 and $r_{av} < 8$mas or C > 0.3 and $r_{av} < 6$ mas. Sources in this intermediate group could be used with cautions.
- **Bad**: contains sources which are not in the other three groups.

Classes of our sources are shown in Table 5.2. The table also contains classification of the sources into calibrator[1] and non-calibrator[2] in the RFC.

[1]A source listed as calibrator in the RFC is a source which has 8 or more detections at both 2.3 and 8.4 GHz, and has position accuracy better than 25 nrad. It is also mentioned in the catalog that this source can be used as a calibrator for interferometers with baselines in the range [1, 10000] km.

[2]A source listed as non-calibrator in the RFC is a source which has at least 8 detections at either 2.3 or 8.4 GHz, and has position accuracy in the range [25, 500] nrad. It is also mentioned in the catalog that a source listed as non-calibrator can be used as a calibrator with care. The classification of the sources, therefore, is based on the source position accuracy, and all the sources in the catalog are known to be relatively compact extragalactic sources.

TABLE 5.2: The average radius r_{av}, class of the sources and status of the sources in the rfc_2013b catalog. C– Calibrator and N– Non-calibrator

Sources	r_{av}	Class	RFC status	Sources	r_{av}	Class	RFC status
0056-572	0.74	Very Good	C	1420-679	2.70	Very Good	N
0252-549	0.85	Very Good	C	1424-418	3.89	Good	C
0312-770	1.50	Very Good	N	1509-564	12.96	Bad	C
0334-546	1.27	Very Good	C	1511-558	3.67	Very Good	C
0454-810	1.66	Very Good	C	1619-680	4.59	Good	C
0530-727	0.70	Very Good	C	1624-617	1.62	Very Good	C
0743-673	1.79	Very Good	C	1659-621	2.35	Very Good	C
0903-573	1.10	Very Good	N	1740-517	9.30	Bad	C
1036-529	4.19	Good	C	1758-651	0.98	Very Good	C
1039-474	1.88	Very Good	C	1806-458	2.32	Very Good	C
1049-534	5.22	Good	C	1831-711	1.49	Very Good	C
1059-631	3.89	Good	C	1903-802	1.30	Very Good	C
1105-680	1.72	Very Good	N	1925-610	6.06	Good	C
1109-567	5.91	Intermediate	N	1935-692	1.54	Very Good	C
1129-580	1.78	Very Good	C	2030-689	0.76	Very Good	C
1143-696	1.15	Very Good	C	2059-786	1.59	Very Good	C
1148-671	5.08	Good	C	2142-758	1.06	Very Good	C
1204-613	15.07	Bad	C	2146-783	1.10	Very Good	N
1249-673	1.84	Very Good	C	2300-683	0.61	Very Good	C
1251-713	1.36	Very Good	C	2333-528	1.27	Very Good	N
1312-533	3.44	Very Good	C	2353-683	1.55	Very Good	C
1352-632	19.30	Bad	N				C

5.3 Comparison of results at 1.6 and 8.4 GHz

In this section we will compare our 1.6 GHz results with those from 8.4 GHz. Of our 43 sources, 35 (see Table 5.2) are known to be good calibrators (i.e have accurate source position and reasonably compact) at 8.4 GHz. If we have a source which is compact at 8.4 GHz observation, it means the size of the source is smaller than the resolution we have at this observing frequency. These small radio source should also be

unresolved at 1.6 GHz for the same array if the spectral index is constant across the source as resolution is related to the frequency (wavelength).

I found that three (1204-613, 1509-564 and 1740-517) of the 35 sources, which are good 8.4 GHz calibrators, are bad calibrators at 1.6 GHz. Therefore, we can say that 91 percent of the sources which are good calibrator at 8.4 GHz are also good calibrator at 1.6 GHz.

Next I will calculate the spectral index of the sources, which can tell us about the mechanisms of the radio emission. I define the spectral index so that

$$S_\nu \propto \nu^{-\alpha}, \tag{5.2}$$

where S is the flux density, α is the spectral index of the sources and ν is the observing frequency. If we have the flux densities of a source at two different frequencies we can estimate the spectral index of the source.

I have determined the spectral index of 20 of my sources for which I have data both at 8.4 and 1.6 GHz, and I found spectral indices between -0.95 to 0.14. The spectral index of the sources is given in Table 5.3.

TABLE 5.3: Spectral index for 20 sources calculated using the flux densities at 8.4 GHz and 1.4 GHz

Sources	α	Sources	α
0056-572	-0.56	1806-458	-0.63
0334-546	-0.44	1831-711	-0.45
0454-810	-0.46	1903-802	-0.19
0530-727	-0.35	1925-610	-0.18
0743-673	0.05	1935-692	0.03
1129-580	-0.68	2030-689	-0.95
1143-696	-0.69	2059-786	-0.56
1148-671	0.14	2142-758	-0.16
1204-613	-0.70	2300-683	-0.85
1619-680	-0.25	2353-686	-0.40
1624-617	-0.51		

Chapter 6

Summary and Conclusion

The first question addressed in this thesis is the suitability of the sources as calibrators for 1.6 GHz observations. The two important properties we need from good calibrator sources are they should be very bright and compact. Concerning the brightness of my sources, the average peak brightness of the 39 sources, which have sufficient flux density (good signal to noise ratio) on all baselines including HartRAO, is 650 mJy per beam with average radius of the beams equal to 2.6 milliarcsecond. With this brightness of the sources we were able to get a signal to noise ratio $\gg 1$. These sources are bright enough to be used as calibrators for VLBI observations.

I used different measures of how compact my sources are. The first one is the core fraction of the sources, and we found that the sources have an average core fraction of 0.89 with median 1.00. The other measure of compactness is the radial extent of the sources. I determined and then averaged three radial extent measurements; the weighted radial extent, 95 percent flux density radius and the HWHM to get an average radius r_{av} for each source.

Using r_{av}, the core fraction and the sources' brightness, we classified the sources into Very good, Good, Intermediate and Bad calibrators (see Table 6.1). Among the 43 sources, I found 31 sources to be very good calibrators, 7 sources to be good calibrators, 1 source to be Intermediate and 4 sources to be bad calibrators for VLBI observations at 1.6 GHz with global baselines.

In addition to compactness and brightness, calibrator sources should have known positions in order to use them for calibration. 35 sources (see Table 5.2) in our sample have accurately determined positions as described in the Radio Fundamental Catalog (RFC) of compact radio sources (see section 4.1), while the remaining 8

sources have only poorly-determined source positions which have large uncertainties because there was not enough data to determine their positions accurately. Therefore, it is important to classify not only the 35 sources but also the 8 sources, because we could get better positions for those 8 sources in future. Out of the 35 sources with accurate positions, 32 sources are sufficiently bright and compact to be used for calibration for 1.6 GHz observations. These 32 sources satisfy all the three criteria (i.e. to be compact, bright and have accurate source position) of calibrator sources to be used for calibration.

My second interest was to figure out how safe it is to use known 8.4 GHz calibrators for 1.6 GHz observations. I made the comparison of results at 1.6 and 8.4 GHz observations using the 35 sources listed as good calibrators for 8.4 GHz observations in the RFC. I found that there is a 91 % chance that a calibrator known to be good at 8.4 GHz can also be safely used at 1.6 GHz observations. Therefore, we can use most of the sources, which are known to be good calibrator at 8.4 GHz but we do not have information about their calibrator quality at 1.6 GHz, for calibration at 1.6 GHz observations.

TABLE 6.1: Class of the sources

Sources	Class	Sources	Class
0056-572	Very Good	1420-679	Very Good
0252-549	Very Good	1424-418	Good
0312-770*	Very Good	1509-564	Bad
0334-546	Very Good	1511-558	Very Good
0454-810	Very Good	1619-680	Good
0530-727	Very Good	1624-617	Very Good
0743-673	Very Good	1659-621	Very Good
0903-573	Very Good	1740-517	Bad
1036-529	Good	1758-651	Very Good
1039-474	Very Good	1806-458	Very Good
1049-534	Good	1831-711	Very Good
1059-631	Good	1903-802	Very Good
1105-680	Very Good	1925-610	Good
1109-567	Intermediate	1935-692	Very Good
1129-580	Very Good	2030-689	Very Good
1143-696	Very Good	2059-786	Very Good
1148-671	Good	2142-758	Very Good
1204-613	Bad	2146-783	Very Good
1249-673	Very Good	2300-683	Very Good
1251-713	Very Good	2333-528	Very Good
1312-533	Very Good	2353-683	Very Good
1352-632	Bad		

Bibliography

Beasley, A. J., Gordon, D., Peck, A. B., Petrov, L., MacMillan, D. S., Fomalont, E. B., & Ma, C. 2002, ApJS, 141, 13

Booth, R. S., de Blok, W. J. G., Jonas, J. L., & Fanaroff, B. 2009, ArXiv e-prints

Clark, B. G. Astronomical Society of the Pacific Conference Series, Vol. 180, , Synthesis Imaging in Radio Astronomy II, ed. G. B. TaylorC. L. Carilli & R. A. Perley, 1

Fanaroff, B. L. & Riley, J. M. 1974, MNRAS, 167, 31P

Fey, A. L. & Charlot, P. 1997, ApJS, 111, 95

—. 2000, ApJS, 128, 17

Fey, A. L., Ojha, R., Jauncey, D. L., Johnston, K. J., Reynolds, J. E., Lovell, J. E. J., Tzioumis, A. K., Quick, J. F. H., Nicolson, G. D., Ellingsen, S. P., McCulloch, P. M., & Koyama, Y. 2004, AJ, 127, 1791

Fey, A. L., Ojha, R., Quick, J. F. H., Nicolson, G. D., Lovell, J. E. J., Reynolds, J. E., Ellingsen, S. P., McCulloch, P. M., Johnston, K. J., Jauncey, D. L., & Tzioumis, A. K. 2006, AJ, 132, 1944

Fomalont, E. B. & Perley, R. A. Astronomical Society of the Pacific Conference Series, Vol. 180, , Synthesis Imaging in Radio Astronomy II, ed. G. B. TaylorC. L. Carilli & R. A. Perley, 79

Fomalont, E. B., Petrov, L., MacMillan, D. S., Gordon, D., & Ma, C. 2003, AJ, 126, 2562

Hungwe, F., Ojha, R., Booth, R. S., Bietenholz, M. F., Collioud, A., Charlot, P., Boboltz, D., & Fey, A. L. 2011, MNRAS, 418, 2113

Johnston, S., Taylor, R., Bailes, M., Bartel, N., Baugh, C., Bietenholz, M., Blake, C., Braun, R., Brown, J., Chatterjee, S., Darling, J., Deller, A., Dodson, R., Edwards, P., Ekers, R., Ellingsen, S., Feain, I., Gaensler, B., Haverkorn, M., Hobbs, G., Hopkins,

A., Jackson, C., James, C., Joncas, G., Kaspi, V., Kilborn, V., Koribalski, B., Kothes, R., Landecker, T., Lenc, A., Lovell, J., Macquart, J.-P., Manchester, R., Matthews, D., McClure-Griffiths, N., Norris, R., Pen, U.-L., Phillips, C., Power, C., Protheroe, R., Sadler, E., Schmidt, B., Stairs, I., Staveley-Smith, L., Stil, J., Tingay, S., Tzioumis, A., Walker, M., Wall, J., & Wolleben, M. 2008, Experimental Astronomy, 22, 151

Kellermann, K. I. & Pauliny-Toth, I. I. K. 1981, ARA&A, 19, 373

Kovalev, Y. Y., Petrov, L., Fomalont, E. B., & Gordon, D. 2007, AJ, 133, 1236

Moran, J. M. & Dhawan, V. Astronomical Society of the Pacific Conference Series, Vol. 82, , Very Long Baseline Interferometry and the VLBA, ed. J. A. ZensusP. J. Diamond & P. J. Napier, 161

NRAO, N. R. A. O. 2014

Ojha, R., Fey, A. L., Johnston, K. J., Jauncey, D. L., Reynolds, J. E., Tzioumis, A. K., Quick, J. F. H., Nicolson, G. D., Ellingsen, S. P., Dodson, R. G., & McCulloch, P. M. 2004, AJ, 127, 3609

Petrov, L., Kovalev, Y. Y., Fomalont, E., & Gordon, D. 2005, AJ, 129, 1163

Petrov, L., Kovalev, Y. Y., Fomalont, E. B., & Gordon, D. 2006, AJ, 131, 1872

—. 2008, AJ, 136, 580

Petrov, L., Phillips, C., Bertarini, A., Murphy, T., & Sadler, E. M. 2011, MNRAS, 414, 2528

Rohlfs, K. & Wilson, T. L. 2004, Tools of radio astronomy

Schneider, P. 2006, Extragalactic Astronomy and Cosmology

Thompson, A. R. Astronomical Society of the Pacific Conference Series, Vol. 180, , Synthesis Imaging in Radio Astronomy II, ed. G. B. TaylorC. L. Carilli & R. A. Perley, 11

Thompson, A. R., Moran, J. M., & Swenson, G. W. 2007, Interferometry and Synthesis in Radio Astronomy, John Wiley & Sons, 2007.

Thompson, W. 1971, Atmospheric transmission handbook: a survey of electromagnetic wave transmission in the earth's atmosphere over the frequency (wavelength) range 3kHz (100km) 3,000 THz (0.1um) (Transportation Systems Center; prepared for National Aeronautics and Space Administration, Washington, D.C.) [LINK]

Wenger, M., Ochsenbein, F., Egret, D., Dubois, P., Bonnarel, F., Borde, S., Genova, F., Jasniewicz, G., Laloë, S., Lesteven, S., & Monier, R. 2000, A&AS, 143, 9

Wohlleben, R., Mattes, H., & Krichbaum, T. 1991, Interferometry in radioastronomy and radar techniques